TECHNISCHE UNIVERSITÄT WIEN

AUTOMATION & CONTROL INSTITUTE
INSTITUT FÜR AUTOMATISIERUNGS- & REGELUNGSTECHNIK

Model-based Thermal Protection Strategy for a Permanent Magnet Synchronous Motor

DIPLOMA THESIS

Conducted in partial fulfillment of the requirements for the degree of a

Diplom-Ingenieur (Dipl.-Ing.)

supervised by

Dipl.-Ing. Martin Baumann
Assoc. Prof. Dr.techn. Andreas Steinböck

submitted at the

TU Wien
Faculty of Electrical Engineering and Information Technology
Automation and Control Institute

by

Andreas Fischer
Matriculation number 11702822

[redacted], February 2024

Complex Dynamical Systems Group
A-1040 Wien, Gußhausstr. 27–29, Internet: https://www.acin.tuwien.ac.at

Vorwort

An erster Stelle danke ich meinen Betreuern, DI Martin Baumann, der mir bei Fragen jederzeit mit schnellem Antworten geholfen hat, und Prof. Andreas Steinböck sowie Prof. Wolfgang Kemmetmüller für wertvolles Feedback und interessante Diskussionen.

Weiters will ich allen Vortragenden des ACIN für die hervorragende Organisation und Durchführung der Lehrveranstaltungen während meines Studiums danken.

Zu guter Letzt gilt mein Dank meinen Freunden und meiner Familie, insbesondere meinen Eltern für ihre durchgehende Unterstützung, die mir diese Ausbildung ermöglicht hat.

[redacted], February 2024

Abstract

For an economic design of electric vehicles, the rated continuous power of the motor is selected according to the typical power requirements. Temporarily allowing the power to exceed the continuous power rating enables to use smaller, cheaper motors with higher utilization under the condition that active thermal power management is used to prevent thermal damage. The present diploma thesis aims at developing a thermal protection algorithm for a permanent magnet synchronous motor used as main drive of an electric vehicle. To take better advantage of the thermal limits, a model-based approach is used. For this purpose, the electrical and thermal characteristics of the motor are modeled. Using model predictive control (MPC), a derating algorithm is developed that systematically considers temperature limits and aging of motor windings at elevated temperatures. It is shown that the developed approach can increase the available motor torque compared to static derating strategies currently used in electric vehicles. The functionality and performance of the developed derating strategy is evaluated using simulation studies.

Kurzzusammenfassung

Für eine wirtschaftliche Entwicklung von Elektrofahrzeugen wird die Motornennleistung entsprechend der typischen Anforderungen an das Fahrzeug gewählt. Zeitlich begrenzt wird eine Spitzenleistung über der Nennleistung zugelassen, wodurch kleinere, billigere Motoren verbaut werden können. Voraussetzung dafür ist jedoch ein aktives thermisches Management, um Schäden am Motor zu verhindern. In dieser Diplomarbeit soll ein thermischer Schutzalgorithmus für eine Permanentmagnetsynchronmaschine, welche als Hauptantrieb eines Elektrofahrzeugs dient, entwickelt werden. Um die thermischen Grenzen besser auszunutzen, wird dafür ein modellbasierter Ansatz verwendet. Dafür werden die elektrischen und thermischen Charakteristiken des Motors modelliert. Es wird ein Derating-Algorithmus entwickelt, der eine modellprädiktive Regelung (MPC) nutzt und damit systematisch die Temperaturgrenzen und die Alterung bei erhöhten Temperaturen berücksichtigt. In der Arbeit wird gezeigt, dass der entwickelte Algorithmus das zur Verfügung stehende Motordrehmoment, im Vergleich zu statischen Derating-Verfahren, wie sie in aktuellen Elektrofahrzeugen verwendet werden, erhöhen kann. Die Funktions- und Leistungsfähigkeit der entwickelten Derating-Strategie wird in Simulationsstudien untersucht.

Contents

List of Figures

List of Tables

1 Introduction

1.1 Motivation

In the last decade, the share of battery electric vehicles (BEV) in the global automotive market significantly increased due to higher availability, improved battery capacities enabling longer ranges, and climate goals that mandate a reduction of internal combustion engine (ICE) vehicles [1]. This raised the interest in the development of electric powertrains, including better models and controllers, to increase efficiency and lower costs.

BEVs can be equipped with different electric motor types, of which permanent magnet synchronous motors (PMSM) and induction motors (IM) are the most prevalent [2]. Typically, a voltage source inverter (VSI) uses the battery voltage to drive the motor currents according to the motor controller. In the motor, the currents generate a mechanical torque through electromagnetic forces. Additionally, there are undesired losses that heat the vehicle components including the battery, power electronics, and the PMSM.

All components have to be designed to withstand the resulting temperatures for a specified lifetime. To improve utilization, it is desirable to use smaller motors with a lower continuous power rating. This rating can be exceeded for limited periods of time, which can temporarily increase the temperatures to potentially dangerous levels and thus cause permanent damage or accelerated aging. Therefore, during operation above the continuous power, a thermal monitoring and protection strategy (derating) has to be used, to prevent excessive temperatures. The derating controller has two main goals. The first, safety-relevant, goal is to protect the motor from exceeding the temperature limits by restricting the available torque. The second goal is to provide enough torque to enable the expected driving performance, especially for acceleration or overtaking maneuvers. A compromise that unites these contradictory goals takes advantage of the typical load profile of motors in vehicles. Most of the time, when driving on roads, the required power is below the continuous power rating (e. g. for keeping a uniform speed). Driving situations for which power above the continuous power rating is required are limited in time, (e. g. accelerating to the desired cruise speed). Using the ability to temporarily exceed the continuous power rating of the motor, a compromise between the two goals can be found.

In this thesis, a model-based thermal protection technique for a PMSM is developed.

1.2 Literature Review

An overview of important derating and temperature monitoring concepts as well as existing thermal models is given in this section.

Driving Cycles

Electric vehicles operate in a wide range of operating conditions, including high accelerations after a stop or during overtaking maneuvers, repeated acceleration and deceleration (e. g. in city traffic), and intervals with low acceleration [3]. These typical drive cycles are considered in the design of electric vehicles by using smaller, cheaper motors that can be temporarily overloaded (operate above their continuous power rating) to achieve higher torque for these maneuvers for a limited time. However, prolonged operation above the continuous power rating causes the motor temperatures to rise, which can lead to damage or accelerate the aging of motor components when thermal limits are exceeded.

Thermal Limits

For PMSMs, the two main components affected by high temperatures are the winding insulation and the permanent magnets. The maximum temperature the insulation can withstand depends on its material properties and is classified according to IEC 60085 [4]. Higher temperatures accelerate the deterioration of the insulation. Its temperature-dependent lifetime can be predicted according to an Arrhenius model [5]. For the permanent magnets, irreversible demagnetization can occur when high temperatures are combined with strong demagnetizing fields. When this occurs, the residual flux density of the magnet is decreased, which reduces the efficiency of the motor and its ability to generate torque [6].

Derating Strategies

To ensure safe operation, the motor temperature is monitored and thermal derating is applied when necessary. Thermal derating means that power and therefore torque are reduced in order to stay within temperature limits. When using derating, there is a compromise between different goals. On the one hand, the motor temperatures have to stay low enough to ensure a sufficiently high motor lifespan and prevent accelerated aging of the winding insulation and demagnetization of the permanent magnets. On the other hand, the power and torque demanded by the driver should be followed closely to provide good driving responsiveness.

The state of the art in production vehicles is to use static derating strategies, which reduce the available torque according to a static relationship above a threshold temperature [7]. This method is an improvement over suddenly shutting off the motor when a temperature limit is reached but often results in conservative behavior and power reductions noticeable to the driver [7].

To avoid these downsides, other, more sophisticated derating strategies were proposed and investigated. In [8], Lemmens et al. integrate a derating algorithm into the current setpoint calculation of a PMSM. Their thermal management strategy monitors the temperature of the stator windings as well as the power electronics, including the insulated-gate bipolar transistors (IGBTs) and freewheeling diodes. The strategy estimates the maximum allowed power losses to keep the temperature within limits. This estimation uses a static equation that contains two terms. The first term is proportional to the difference of the temperature to its limit. The second term contains the permitted power

losses for steady-state operation at a constant temperature. The current limit in the setpoint calculation is then derived from the estimated maximum power loss. A potential drawback is that only the losses and resulting temperatures in the stator windings are considered. Other losses, e. g. due to eddy currents, and the rotor temperatures are not considered.

Additionally, the dynamic thermal behavior of the motor can be considered to improve performance. In [9], Calzo et al. use a PI controller to limit the available current for protecting the PMSM from high temperatures. The controller uses the difference between the motor temperature and a temperature threshold, above which derating should start, as input. The controller features an anti-windup strategy and outputs a factor, in the range [0, 1], that limits the torque-producing motor current. The described approach additionally protects the power electronics from high temperatures. The current modulation technique and switching frequency are changed using a hysteresis controller. In the measured results, an oscillation of the temperature is observable, however, the authors do not explain if this is due to the PI controller or the hysteresis.

Model predictive control (MPC), also known as receding horizon control (RHC), allows a systematic consideration of the model and the constraints. Grüne and Pannek [10] cover the topic of MPC in detail. MPC is a model-based control method that solves an optimization problem, consisting of a cost function and constraints that model the system dynamics and limits of the state and input, to find the optimal system inputs, satisfying the constraints.

In [11], Wallscheid and Böcker use MPC-based derating under the assumption that the future course of the track is known. The cost function contains the time required to finish the track as well as the amount of mechanical braking, thus improving efficiency by using more electrical recuperation. A similar approach, for real-time operation in a vehicle, is implemented in [12] by Winkler et al.. This approach improves lap times as well as energy efficiency compared to a static derating strategy. An MPC for speed control is used, for which the cost function contains the tracking error in terms of a track-position-dependent desired speed. In both papers [11] and [12], a one-dimensional mechanical vehicle model for the position and velocity is used, the temperature limits are enforced through optimization constraints, and knowledge of the complete future track is assumed. However, in real driving situations, the future course and desired speed are rarely known to the vehicle controller. An approach without future track knowledge by Sun et al. is detailed in [13]. Because no information about the upcoming desired velocity is available, the future motor speed is assumed constant in the prediction horizon. Similar to the approach by Lemmens et al. [8], the maximum permissible copper losses satisfying the constraints are calculated in [13]. This calculation is performed using a linear MPC with a cost function that minimizes the difference of the motor temperature to its limit. The resulting maximum losses are then used to determine the motor current and torque limits. As in the methods by Lemmens et al. [8], a downside of this approach is that only the copper losses are considered. There is no clear way how other effects, such as eddy losses, can be incorporated into this approach.

Thermal Monitoring

For thermal protection methods, knowledge of the temperatures in the PMSM is usually necessary. Wallscheid [14] gives an overview of how the thermal state of electric motors can be determined: Placing temperature sensors within the motor is often not economically viable. Therefore, the temperatures have to be monitored using different methods, which can be categorized into direct and indirect methods. Indirect methods use temperature-sensitive electrical quantities to make conclusions about the motor temperatures. However, indirect methods do not allow monitoring temperatures at specific locations but only average component temperatures [15]. Direct methods use a thermal model of the motor based on the heat equation. In the papers [11], [12], and [13], which use MPC for derating, the thermal dynamics of the PMSM are modeled using lumped-parameter thermal networks (LPTNs) with two to four nodes. LPTNs represent the motor as a thermal equivalent circuit consisting of thermal resistors, capacitors, voltage sources, and current sources. Another approach is to use model-order reduction of a high-dimensional finite volume model of the motor to make it suitable for real-time use [15]. This thesis uses a thermal model based on the reduced-order model presented by Baumann et al. [15].

Road Parameter Estimation and Prediction

To substitute the unavailable knowledge about the future track and desired speed required by the MPC-based derating approaches in [11] and [12], a prediction of these future quantities can be used. This prediction is based on the current vehicle state, desired torque, and road parameters. Many road parameters cannot be directly measured and have to be estimated from other measurements. Extensive investigations of parameter estimation for vehicles exist in the literature. Road slope estimation based on a longitudinal vehicle model is implemented in [16] and using a Kalman Filter (KF) in [17]. A combined road slope and vehicle mass estimation approach is presented in [18], using an adaptive observer-based approach. In [19], an Extended Kalman Filter (EKF) for estimating road slope and vehicle mass is combined with active modification of the motor torque, which can improve parameter identifiability.

Based on the estimated current parameters, the prediction provides the future quantities required by the MPC-based derating approaches. It bridges the gap between the approach in [13] which assumes no future knowledge and assumes the future quantities to be constant and the approaches in [11] and [12] which require full knowledge of the future road slope and desired speed.

1.3 Objectives

The aim of this thesis is to develop an algorithm for thermal protection of an interior PMSM of a BEV for better utilization of the thermal limits of the motor compared to static derating strategies. In contrast to the MPC-based derating algorithms presented in [11] and [12], it should apply to situations where the future course of the track and actions of the driver are not exactly known. However, the algorithm may internally predict the track and the driver's actions. This should be superior to the naive approach, used in [13],

which assumes them to be constant. For this prediction, only sensors that are typically available in standard BEVs should be used.

In detail, the following topics are addressed:

- Model the vehicle motion according to models available in the literature. Model the temperature of the motor based on an existing thermal model [15].
- Develop and implement an MPC-based derating algorithm to prevent thermal overload of the motor.
- For the MPC, formulate the optimization problem appropriate for thermal protection of the PMSM in the vehicle.
- In the MPC, incorporate the cumulative thermal aging of the stator windings (cf. [5]) into the derating decision.
- Validate the designed algorithm using simulation studies and compare it to state-of-the-art thermal protection strategies.

1.4 Structure

The remaining thesis has the following structure:

Chapter 2 describes the mathematical model of the vehicle, electrical and thermal parts of the PMSM, and cooling. It also contains the parameter and state estimation method used and explains the thermal aging model to predict the temperature-dependent lifetime of the stator windings. Additionally, the model used in the MPC optimization is explained, which is based on the full mathematical model and includes some reductions in favor of real-time execution.

In Chapter 3, the MPC-based derating algorithm is described and the underlying optimization problem is formulated and discussed. The derating algorithm allows for different approaches to predict the torque and speed in the prediction horizon. A method to predict the future quantities for motor speed and desired torque based on available sensor data and an observer for the road slope is presented. Additionally, the naive assumption of constant quantities and the unrealistic assumption of exactly known future trajectories are implemented for comparison.

Chapter 4 presents simulation results of the developed derating algorithms and compares them to the results of existing derating strategies. Based on the simulation of various drive cycles, this includes a validation that the temperature limits are satisfied and a quantitative comparison of the quality of the derating strategies. Moreover, the effects of the different prediction approaches used in the MPC are compared.

Finally, Chapter 5 summarizes the main findings and gives an outlook on possible extensions of the work.

2 Modeling

In this chapter, the mathematical model used for the controller and the simulation is presented. The focus lies on accurately modeling the thermal behavior, which is necessary for a well-performing, model-based derating algorithm.

The model consists of several parts. The thermal model (Section 2.4) describes the temperature field in the motor based on the heat equation. Power losses and temperatures of cooling fluids serve as inputs of this model. Section 2.5 explains the temperature limits and thermal aging of the motor windings. The models for the water and oil cooling circuits, the heat exchanger and the oil sump (Section 2.3) are needed to calculate the temperatures of the cooling water and oil. The electrical model of the PMSM (Section 2.1) is used for calculating the setpoint currents of the motor for a desired torque. The loss model (Section 2.2) uses the calculated currents to determine the electromagnetic losses of the PMSM. Finally, the mechanical model (Section 2.6) ties the internal motor speed and torque to the vehicle speed and acceleration. The electrical-, loss-, cooling- and thermal-models are based on [15].

2.1 Electrical Model

PMSMs are often applied in industry as well as electric vehicles due to their high efficiency and power density. In this work, a three-phase interior PMSM with the specification outlined in Table 2.1 is considered.

Parameter		Value	
continuous power rating		∼100	kW
maximum motor speed	n_{lim}	16500	rpm
number of pole pairs	p	4	

Table 2.1: Electrical parameters of the PMSM.

The nonlinear model of the PMSM is represented in the rotor-fixed d/q reference frame [20] and is given by

$$\dot{\boldsymbol{\Psi}}_s = -R_s\,\mathbf{i}_s + \boldsymbol{\Omega}_e\,\boldsymbol{\Psi}_s + \mathbf{u}_s \tag{2.1}$$

with the current $\mathbf{i}_s$, flux linkage $\boldsymbol{\Psi}_s$, and voltage $\mathbf{u}_s$ each represented as $\mathbf{x}_s = \begin{bmatrix} x_d & x_q \end{bmatrix}^{\mathrm{T}}$ and the antisymmetric matrix $\boldsymbol{\Omega}_e = \omega_e \begin{bmatrix} 0 & 1 \\ -1 & 0 \end{bmatrix}$. The electrical angular velocity is $\omega_e = 2\pi\, n\, p$ with the mechanical speed n of the rotor and the number p of pole pairs. The electrical

resistance of the stator coils is modeled in the form

$$R_s = R_{s,\mathrm{ref}}\Big[1 + \alpha_{\mathrm{Cu}}\left(T_{\mathrm{Cu}} - T_{\mathrm{ref}}\right)\Big]\, k_{ac}(\omega_e,\, T_{\mathrm{Cu}}) \ . \tag{2.2}$$

Its dependencies on the average copper temperature T_{Cu} and the electrical angular velocity ω_e are modeled using a linear coefficient of temperature α_{Cu} and the AC resistance factor $k_{ac}(\omega_e, T_{\mathrm{Cu}})$, which includes proximity and skin effects in the winding. $R_{s,\mathrm{ref}}$ is the DC stator resistance at the reference temperature T_{ref}. To include saturation and cross-coupling effects as well as the dependence of the magnetic flux on the permanent magnet temperature T_{pm}, the flux linkages Ψ_d and Ψ_q in (2.1) are functions of the currents (i_d, i_q) and T_{pm}. These functions for flux linkages and stator resistance are implemented as lookup tables which are populated based on measurements and finite element analyses of the motor. The electromagnetic torque M produced by the PMSM [20] is

$$M = \frac{3p}{2}(i_q\,\Psi_d - i_d\,\Psi_q) \ . \tag{2.3}$$

The mechanical motor speed n and torque M are limited

$$|n| \leq n_{\mathrm{lim}} \tag{2.4a}$$
$$|M| \leq M_{\mathrm{lim}}(|n|) \tag{2.4b}$$

to prevent mechanical damage to the shaft. Figure 2.1 shows the torque limit function (2.4b). The maximum torque is constant below $n = 4500\,\mathrm{rpm}$, and then follows a curve that is approximately proportional to $1/n$.

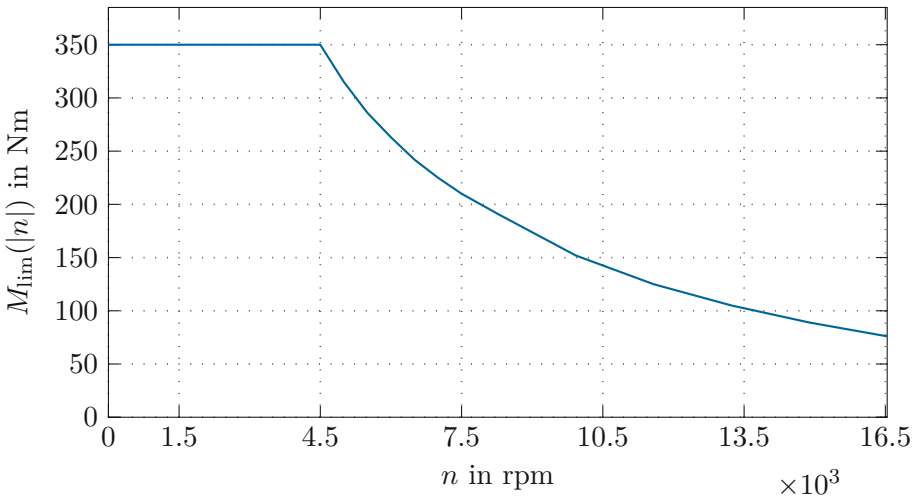

Figure 2.1: Torque limit function $M_{\mathrm{lim}}(|n|)$.

The battery dynamic is not modeled and a constant supply voltage is assumed. Powered by the battery, the voltage source inverter (VSI) drives the motor voltages u_d and u_q, which are therefore limited

$$\|\mathbf{u}_s\|_2 \leq u_{\mathrm{lim}}(n) \tag{2.5}$$

with the maximum voltage magnitude $u_{\lim}(n)$.

To find the optimal current $\mathbf{i}_s^*$ such that torque M according to (2.3) equals a desired torque M_d while minimizing the current magnitude and satisfying the voltage constraints (2.5), the optimization problem

$$\min_{\mathbf{i}_s} \quad J(\mathbf{i}_s) = \|\mathbf{i}_s\|_2^2 \tag{2.6a}$$

$$\text{s.t.} \quad \mathbf{g}_1(\mathbf{i}_s) = -R_s\,\mathbf{i}_s + \boldsymbol{\Omega}_e\,\boldsymbol{\Psi}_s + \mathbf{u}_s = \mathbf{0} \tag{2.6b}$$

$$g_2(\mathbf{i}_s) = M - M_d = 0 \tag{2.6c}$$

$$h(\mathbf{i}_s) = \|\mathbf{u}_s\|_2 - u_{\lim}(n) \leq 0 \tag{2.6d}$$

is formulated and solved. In (2.6b), the quasi-static case $\dot{\boldsymbol{\Psi}}_s = \mathbf{0}$ is considered. The

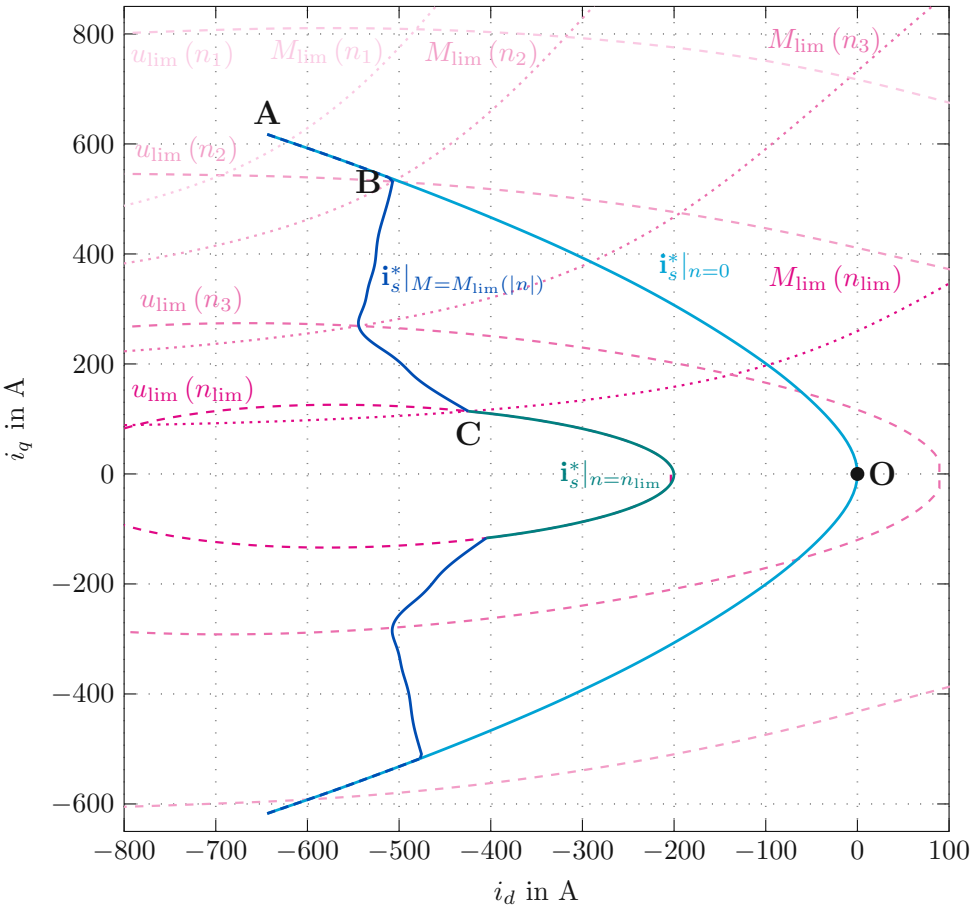

Figure 2.2: Visualization of the optimal solution $\mathbf{i}_s^*$ of (2.6). For selected motor speeds n_i ($i = 1, 2, 3, \lim$), the dotted lines show the maximum motor torque and the dashed lines show the voltage limit. For a given motor speed n and desired torque M_d, the current $\mathbf{i}_s^*$ must lie on the constant torque line $M(n) = M_d$ and within the voltage limit $u_{\lim}(n)$.

desired torque M_d must satisfy the torque limit (2.4b).

The solution $\mathbf{i}_s^*$ of the optimization problem (2.6) is visualized in the i_d-i_q-plane in Figure 2.2. The blue lines show the optimal current setpoint $\mathbf{i}_s^*$. For motor speed $n = 0$, the optimal setpoint for the currents starts at the origin O and follows the light blue maximum torque per ampere (MTPA) curve ($\mathbf{i}_s^*|_{n=0}$) for increasing torque until point A at which the maximum torque is reached. When choosing a setpoint on this line, the current magnitude is minimized for a given torque.

When the motor speed is increased, the maximum torque gets limited according to the torque limit function (2.4b), cf. Figure 2.1. The optimal currents stay at point A until the maximum torque gets reduced due to the increasing speed. First, the dark blue line ($\mathbf{i}_s^*|_{M=M_{\lim}(|n|)}$) follows the MTPA curve back with decreasing torque until point B. At this point, the voltage limit $u_{\lim}(n)$ comes into effect. To increase the speed further, field weakening is used to partially compensate the magnetic flux of the permanent magnets. The curve of optimal current selection then follows the intersection points of the torque limit and voltage limit curves of the respective motor speed n. At point C the motor speed limit $n_{\lim}$ is reached.

The teal line ($\mathbf{i}_s^*|_{n=n_{\lim}}$) shows the optimal current setpoint at the maximum motor speed for varying torque. For negative torque, the curves have a similar shape with $i_q < 0$. For any given motor speed n and torque M, the optimal current setpoint is located in the area enclosed by the blue lines.

For specific motor speeds (n_1, n_2, n_3, and $n_{\lim}$), the voltage limit curves $u_{\lim}(n)$ are displayed as dashed lines and the maximum torque curves $M_{\lim}(|n|)$ as dotted lines.

2.2 Loss Model

The loss model uses the currents i_d, i_q, and the electrical frequency ω_e to calculate the electromagnetic losses and assign them to different parts of the motor. There are ohmic copper losses in the windings, iron losses from magnetic hysteresis and eddy currents in the rotor and the stator iron, and losses in the permanent magnets. The copper losses

$$P_{\mathrm{Cu}} = \frac{3}{2} R_s \left\|\mathbf{i}_s\right\|_2^2 \tag{2.7}$$

depend on the magnitude of the current $\|\mathbf{i}_s\| = \sqrt{i_d^2 + i_q^2}$. The hysteresis losses are proportional to the electrical angular frequency ($P_{\mathrm{hyst}} \propto \omega_e$) and the eddy-current losses are proportional to the square of this frequency ($P_{\mathrm{eddy}} \propto \omega_e^2$) [21]. The total losses in the stator are modeled in the form

$$P_t = \omega_e W_{t,\mathrm{hyst}}(i_d, i_q) + \omega_e^2 W_{t,\mathrm{eddy}}(i_d, i_q) \tag{2.8a}$$

$$P_y = \omega_e W_{y,\mathrm{hyst}}(i_d, i_q) + \omega_e^2 W_{y,\mathrm{eddy}}(i_d, i_q)\ . \tag{2.8b}$$

The stator losses are separated into losses in the stator teeth P_t and the yoke P_y. The total losses in the permanent magnets and the rotor can be described by

$$P_{\mathrm{pm}} = P_{\mathrm{pm}}(i_d, i_q, \omega_e) \tag{2.9a}$$

$$P_r = \omega_e W_{r,\mathrm{hyst}}(i_d, i_q) + \omega_e^2 W_{r,\mathrm{eddy}}(i_d, i_q)\ . \tag{2.9b}$$

The factors $W_x(i_d, i_q)$ and $P_{\text{pm}}(i_d, i_q, \omega_e)$ are nonlinear functions determined by finite element analyses. The losses P_{Cu}, P_y, P_t, P_{pm}, and P_r serve as inputs of the thermal model discussed in Section 2.4.

2.3 Cooling Model

Apart from the electromagnetic losses, the motor temperature is influenced by a dedicated cooling system. There are two cooling circuits, one with water and one with oil. They are coupled via a heat exchanger to transfer heat between the oil and the water circuit. The water cools the voltage source inverter before it passes through the heat exchanger and then the cooling jacket of the PMSM. The oil is pumped from an oil sump, through the heat exchanger using an internal pump. Finally, it is sprayed through nozzles onto the end-windings and via a lance into the hollow rotor shaft. The oil is then collected again in the sump.

It is assumed that the water flow Q_w and the water inlet temperature to the heat exchanger $T_{w,\text{in}}$ are held constant. The oil pump is a fixed displacement pump that is driven by the PMSM. Therefore, the oil flow rate is a linear function of the motor speed $Q_{\text{oil}} = Q_{\text{oil}}(n)$.

2.3.1 Heat Exchanger

A stationary heat exchanger model is used that calculates the thermal power transferred from the cooling water to the oil in the form

$$P_{\text{hx}} = (T_{w,\text{in}} - T_{\text{sump}})\alpha_{\text{hx}}(Q_{\text{oil}}, Q_w) \tag{2.10}$$

depending on the flow rates Q_w and Q_{oil}, the input temperatures $T_{w,\text{in}}$ and T_{sump}, and the heat transfer coefficient $\alpha_{\text{hx}}(Q_{\text{oil}}, Q_w)$. The temperature of the oil entering the heat exchanger is the same as the oil sump temperature T_{sump}. The output temperatures

$$T_w = T_{w,\text{in}} - \frac{P_{\text{hx}}}{Q_w\, \rho_w\, c_{p,w}} \tag{2.11a}$$

$$T_{\text{oil}} = T_{\text{sump}} + \frac{P_{\text{hx}}}{Q_{\text{oil}}\, \rho_{\text{oil}}\, c_{p,\text{oil}}} \tag{2.11b}$$

follow from the first law of thermodynamics.

2.3.2 Oil Sump

The dynamics of the oil sump temperature are modeled assuming a spatially homogenous temperature T_{sump}. From the first law of thermodynamics

$$\dot{T}_{\text{sump}} = \frac{1}{C_{\text{oil}}}(P_{\text{ew,oil}} + P_{s,\text{oil}} + P_{\text{hx}} + P_{\text{gbx}} + P_{\text{amb}}) \tag{2.12}$$

follows. The power from the end-windings $P_{\text{ew,oil}}$ and from the shaft $P_{s,\text{oil}}$ are determined in (2.23) using the thermal motor model described in Section 2.4.

Mechanical losses are considered in the form

$$P_{\text{gbx}} = (1 - k_{\text{gbx}})\, n\, M \tag{2.13}$$

using a gearbox efficiency factor k_{gbx}. Cooling of the sump through the housing by ambient air with the temperature T_{amb} is modeled in the form

$$P_{\text{amb}} = (T_{\text{amb}} - T_{\text{sump}})\alpha_{\text{amb}} \tag{2.14}$$

with the heat transfer coefficient α_{amb}. The ambient temperature T_{amb} is considered constant. The factors k_{gbx}, and α_{amb}, as well as the thermal capacity C_{oil} of the oil in the oil sump have been identified from measurements [15].

2.4 Thermal Motor Model

The thermal model is the centerpiece of the model and its accuracy is important for a reliable operation of the developed derating algorithm. The model captures the thermal dynamics of the PMSM based on the inputs from the electrical (Section 2.1), loss (Section 2.2), and cooling (Section 2.3) sub-models.

2.4.1 Thermal Modeling

Wallscheid [14] provides a summary of thermal modeling strategies for electrical motors. Due to the complex thermal behavior and complex geometries, there are different types of models:

Black-box models do not include any prior information and are trained based on measurement or simulation data. Recently, especially machine learning techniques have been increasingly used to create black-box thermal models.

Gray- or white-box models are based on physical equations. For the considered application, the heat equation

$$\rho c_p \frac{\mathrm{d}T}{\mathrm{d}t} = \nabla \cdot (\lambda \nabla T) + g \ , \tag{2.15}$$

i. e. a partial differential equation (PDE), is the basis for the model, where ρ, c_p, and λ are the mass density, specific heat capacity, and thermal conductivity, respectively, of the material. To get a model that can be numerically evaluated, spatial discretization may be applied to transform the PDE into ordinary differential equations (ODEs).

Finite element and finite volume methods typically use a fine mesh to capture spatial details. The resulting high-dimensional system of equations is often not suitable for real-time evaluation, especially on embedded computers. Model reduction techniques can be used to simplify these models while retaining the properties and dynamics that are of interest [22].

Lumped-parameter thermal networks (LPTNs) are the thermal counterpart to electrical equivalent circuits [14]. Every node of the circuit is associated with a temperature state (analogous to an electrical potential) of the dynamic system. The nodes are connected with edges consisting of thermal resistors, thermal capacitors, or thermal sources. The thermal sources are the system inputs and represent losses (analogous to electrical current sources) and external temperatures (analogous to electrical voltage sources).

2.4.2 Reduced-Order Model

The thermal model of the PMSM used in this thesis is a reduced-order model developed by Baumann et al. [15]. It is based on the heat equation (2.15) and discretization using the finite volume method. In the full finite volume model, the state $\mathbf{x}_f$ consists of the temperatures of the individual finite volumes. The state space representation of this nonlinear system is

$$\mathbf{M}\dot{\mathbf{x}}_f = \mathbf{A}\mathbf{x}_f + \sum_{k=1}^{N_G} G_k(\mathbf{p}_s,\, n)\mathbf{N}_k\mathbf{x}_f + \mathbf{B}\begin{bmatrix}\mathbf{q}(\mathbf{p}_s)\\ \mathbf{g}(\mathbf{u},\, \mathbf{C}_{\text{avg}}\mathbf{x}_f)\end{bmatrix}, \tag{2.16}$$

with the thermal mass matrix $\mathbf{M}$, constant matrices $\mathbf{A}$, $\mathbf{N}_k$, and $\mathbf{B}$, thermal conductances $G_k(\mathbf{p}_s,\, n)$ for $k \in [1,\, N_G]$, with the number of thermal conductances N_G. The system inputs are $\mathbf{q}(\mathbf{p}_s)$, which represents part of the heat flows across the boundaries to the cooling fluids, and the electromagnetic losses $\mathbf{g}(\mathbf{u}, \mathbf{C}_{\text{avg}}\mathbf{x}_f)$. The inputs themselves depend on

$$\mathbf{p}_s = \begin{bmatrix} Q_w & T_w & Q_{\text{oil}} & T_{\text{oil}}\end{bmatrix}^{\text{T}}, \tag{2.17}$$

$$\mathbf{u} = \begin{bmatrix} i_d & i_q & n\end{bmatrix}^{\text{T}}, \tag{2.18}$$

and averaged component temperatures $\mathbf{C}_{\text{avg}}\mathbf{x}_f$.

Using model reduction, a simpler model that can be evaluated in real-time was derived from the high-dimensional finite volume model (2.16) [23], [22]. This reduced-order model (ROM) is a ten-dimensional nonlinear system with the thermal state $\mathbf{x}_t$. Contrary to the full model or LPTNs, the states do not correspond to actual temperatures of the motor. However, interpretable physical temperatures are obtained from the output equation (2.19b).

The state space representation of the reduced-order model is

$$\mathbf{M}_r\dot{\mathbf{x}}_t = \mathbf{A}_r(\mathbf{p}_s,\, n)\mathbf{x}_t + \mathbf{B}_r\begin{bmatrix}\mathbf{q}(\mathbf{p}_s)\\ \mathbf{g}(\mathbf{u},\, \mathbf{C}_{r,\text{avg}}\mathbf{x}_t)\end{bmatrix} \tag{2.19a}$$

$$\mathbf{y} = \mathbf{C}\,\mathbf{x}_t = \begin{bmatrix} T_{\text{Cu}} & T_{\text{pm}} & T_{\text{ew,le}} & T_{\text{ew,ole}}\end{bmatrix}^{\text{T}}, \tag{2.19b}$$

where

$$\mathbf{x}_f \approx \mathbf{V}\mathbf{x}_t\,, \tag{2.20}$$

$$\mathbf{A}_r(\mathbf{p}_s,\, n) = \mathbf{W}^{\text{T}}\left(\mathbf{A} + \sum_{k=1}^{N_G} G_k(\mathbf{p}_s,\, n)\mathbf{N}_k\right)\mathbf{V}\,, \tag{2.21}$$

and

$$\mathbf{B}_r = \mathbf{W}^{\text{T}}\mathbf{B} \tag{2.22}$$

with projection matrices $\mathbf{W}$ and $\mathbf{V}$ from the model reduction. The output matrix $\mathbf{C}$ is used to calculate the representative temperatures of the active windings T_{Cu}, permanent magnet T_{pm}, and end-windings on the lead-end and opposite-lead-end side, $T_{\text{ew,le}}$ and $T_{\text{ew,ole}}$.

The thermal powers transferred from the end-windings $P_{\mathrm{ew,oil}}$ and shaft $P_{s,\mathrm{oil}}$, respectively, to the cooling oil,

$$P_{\mathrm{ew,oil}} = P_{\mathrm{ew,oil}}(\mathbf{x}_t, T_{\mathrm{oil}}) \tag{2.23a}$$

$$P_{s,\mathrm{oil}} = P_{s,\mathrm{oil}}(\mathbf{x}_t, T_{\mathrm{oil}}) \ , \tag{2.23b}$$

are functions of the thermal state $\mathbf{x}_t$ and oil temperature T_{oil}.

2.5 Thermal Limits, Degradation, and Damage

In addition to influencing the electrical and thermal properties of the PMSM, high temperatures can cause damage or accelerated aging if they exceed certain thresholds. There are two main reasons for temperature limits in PMSMs: demagnetization of the permanent magnet and degradation of the winding insulation.

When a strong magnetic field opposing the magnetization direction of a permanent magnet is applied, demagnetization may occur. This demagnetization behavior is temperature dependent. With higher temperatures, lower field strengths are required for demagnetization [6]. In the design phase of PMSMs, permanent magnets are selected according to the rated operating temperatures of the motor [24]. Therefore, the maximum permanent magnet temperature is considered a hard limit. In addition to the demagnetization behavior, the magnet temperature influences the motor efficiency because the residual flux density is temperature-dependent with a negative temperature coefficient [6].

The second reason for thermal limits are aging effects of the winding insulation. According to [25], this degradation can be modeled as follows. The insulation consists of polymers that electrically insulate the wires against each other and against the iron. Chemical processes in the polymers deteriorate the quality until electrical faults occur. With higher temperature T, the deterioration rate increases, which decreases the lifetime $L(T)$ according to the Arrhenius-Dakin equation

$$L(T) = A \exp\left(\frac{B}{T}\right) \tag{2.24}$$

where A and B are material-dependent constants [25]. Madonna et al. [5] identified these parameter values for PMSM windings using accelerated thermal aging tests. Their results are given in Table 2.2. In these experimental tests, sample windings are heated to

Parameter	Value	
A	$4.48 \cdot 10^{-12}$	h
B	17 030	K

Table 2.2: PMSM winding lifetime parameters.

temperature levels far above the normal point of operation to make them fail in short timespans. From the observed lifespans at high temperatures, the parameters A and B in (2.24) are estimated.

In (2.24), T is a constant temperature. To model the effect that a time-varying temperature profile has on the lifetime, the so-called loss of life function [5]

$$LF(T(\cdot), t) = \int_{t_0}^{t} \frac{1}{L(T(\tau))} \, \mathrm{d}\tau \tag{2.25}$$

is used. It calculates the fraction of the lifetime that is lost during the time interval $t \in [t_0, t]$. This approach represents a cumulative damage model.

In addition to faster degradation of the winding insulation, high winding temperatures negatively affect the motor efficiency. Due to temperature-dependent properties of the electrical conductors, e. g. the positive temperature coefficient of resistance $\alpha_{\mathrm{Cu}} > 0$, the losses are greater at higher winding temperatures. Therefore, lower stator winding temperatures are preferred.

2.6 Mechanical Model

To characterize the dynamics of the vehicle, a longitudinal vehicle model

$$\begin{aligned} \dot{s} &= v \\ \dot{v} &= \frac{1}{m_{\mathrm{eff}}}(F_a - F_d - F_r - F_g) \end{aligned} \tag{2.26}$$

similar to that in [11] is used, with the vehicle position s and speed v. An effective mass

$$m_{\mathrm{eff}} = m + \frac{J}{r_w^2} \tag{2.27}$$

includes the vehicle mass m and the influence of the moment of inertia J of the rotating masses (e. g. wheels and shafts). It is assumed that there is no slip along the power train (motor, gearbox, wheel-street interface, ...) so that the mechanical motor speed n of the PMSM and vehicle speed v are related by

$$v = \omega_m \frac{r_w}{i_{\mathrm{gbx}}} \tag{2.28}$$

with the gearbox ratio i_{gbx} and the wheel radius r_w. The driving force

$$F_a = M \frac{i_{\mathrm{gbx}}}{r_w} \tag{2.29}$$

is proportional to the motor torque M from (2.3). The other external force terms in (2.26) are the drag force F_d, the friction force F_r, and the gravitational force along the road slope F_g. Assuming no wind, the drag force

$$F_d = \frac{1}{2} \rho_a \, c_d \, A_d \, v^2 \tag{2.30}$$

is proportional to the square of the vehicle speed v using the density of air ρ_a, vehicle drag coefficient c_d, and cross-sectional area A_d. For simplicity, only positive speeds are

considered, which implies $F_d \geq 0$. Considering simple rolling friction, the road slope γ and the friction coefficient c_r, the friction force follows as

$$F_r = c_r m g \cos(\gamma) \ . \tag{2.31}$$

The gravitational force along the road slope is modeled in the form

$$F_g = m g \sin(\gamma) \ . \tag{2.32}$$

Table 2.3 lists all parameters of the mechanical model. The values for vehicle mass, cross-sectional area, and drag coefficient correspond to values of a typical electric SUV. The rolling friction coefficient c_r is chosen as a typical value for tires on concrete.

Parameter		Value	
Vehicle mass	m	2200	kg
Effective mass	m_{eff}	2500	kg
Vehicle cross-sectional area	A	2.78	m^2
Drag coefficient	c_d	0.29	
Rolling friction coefficient	c_r	0.01	
Wheel radius	r_w	0.38	m
Gearbox ratio	i_{gbx}	11.3	
Air density	ρ_a	1.2	kg/m^3
Gravitational acceleration	g	9.81	m/s^2

Table 2.3: Parameters of the longitudinal mechanical vehicle model.

2.7 Assembled Model

Figure 2.3 displays a diagram of the assembled model. The state of the complete model consists of the vehicle position s, the vehicle speed v, the oil sump temperature T_{sump}, and the thermal state $\mathbf{x}_t$ of the reduced-order model. The model inputs are the desired torque M_d, the road slope γ, the water inlet temperature $T_{w,\text{in}}$, and the water flow Q_w.

For the simulation and use in the controller, the model is discretized using the forward Euler method with the sampling time $t_s = 0.1\,\text{s}$.

For the MPC-based derating algorithm explained in Chapter 3, the motor model has to be repeatedly calculated to solve the optimal control problem (OCP). Therefore, it is important that the model can be efficiently evaluated. The thermal model takes the longest to evaluate of all models used in the algorithm. To improve the computational efficiency, the following measures are implemented:

First, the optimal current setpoints according to (2.6) are stored in a lookup table, so that (2.6) does not have to be solved online. The optimal currents are then computed by linear interpolation in the form

$$\mathbf{i}_s^* = \mathbf{f}_{\text{ops}}(M, \omega_e, T_{\text{Cu}}, T_{\text{pm}}) \ , \tag{2.33}$$

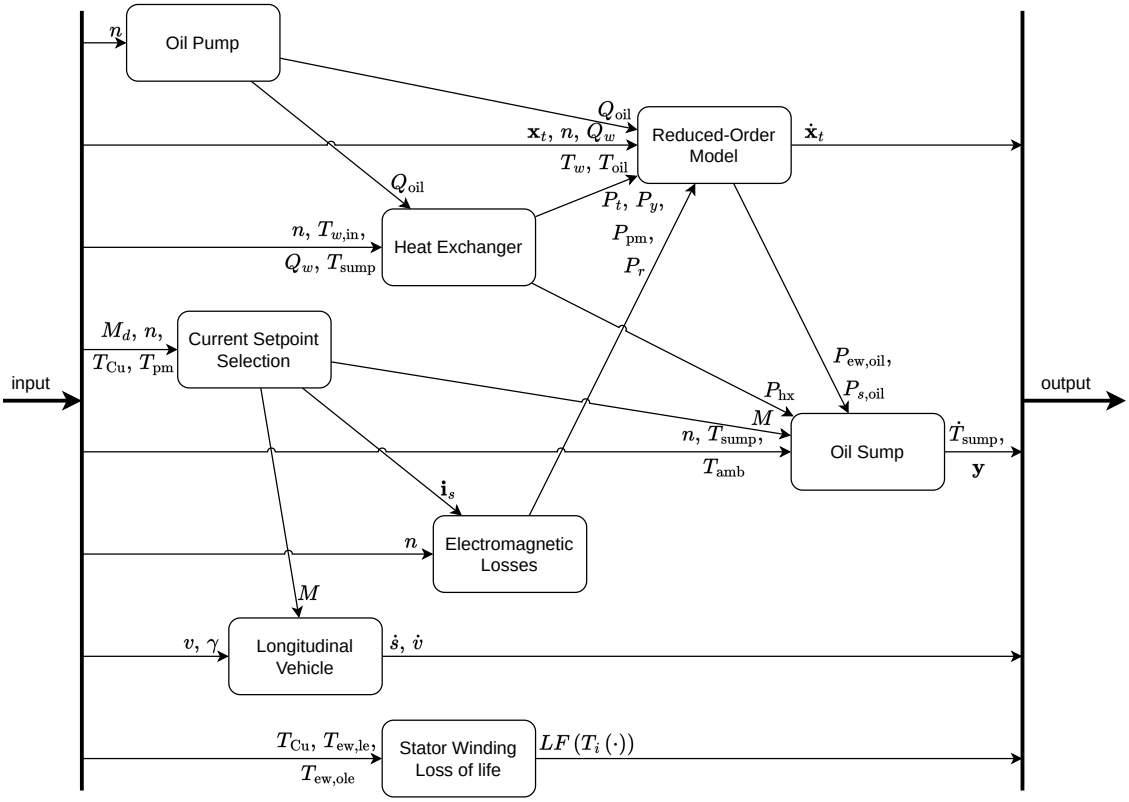

Figure 2.3: Assembled model

as functions of the motor torque M, the electrical frequency ω_e, the active winding temperature T_{Cu}, and the magnet temperature T_{pm}.

Secondly, the thermal conductances $G_k(\mathbf{p}_{s,k},\, n_k)$ and the values $\mathbf{p}_{s,k}$ in (2.16) related to the cooling model are assumed to be constant within the whole prediction horizon. Therefore, the cooling model (Section 2.3) does not have to be evaluated when solving the OCP. Additionally, the system matrix $\mathbf{A}_{r,k} = \mathbf{A}_r(\mathbf{p}_{s,k},\, n_k)$ and heat flows to the cooling fluids $\mathbf{q}_k = \mathbf{q}(\mathbf{p}_{s,k})$ in (2.19a) have to be calculated only once per prediction horizon.

3 Optimization and Derating Algorithm

This chapter describes the developed MPC-based derating algorithm as well as the underlying optimization problem. Based on the models from Chapter 2, the individual parts of the derating algorithm are explained. The optimization problem is formulated such that it protects the motor components from thermal damage and accelerated aging. For this purpose, the temperature-dependent deterioration of the windings is quantitatively modeled, road parameters are estimated, and the future vehicle speed as well as desired torque are predicted.

3.1 Thermal Limits

Section 2.5 explains how operation with elevated temperatures can negatively impact the motor. Most importantly, there are temperature limits for the stator windings and the permanent magnet in order to avoid damage and rapid deterioration of the PMSM. Additionally, the motor efficiency is influenced by the temperatures, mainly because of the temperature-dependent stator resistance and permanent magnet flux. However, the primary goal of this work is thermal protection of the motor. Efficient operation is thus left as a task for the speed controller or vehicle driver and is of minor concern.

The lifetime of the windings depends on the temperature profile they are exposed to. This effect is modeled using the loss of life function (2.25). The thermal model (Section 2.4) has three outputs related to the stator: the copper temperature $y_1 = T_{\mathrm{Cu}}$, the lead-end end-winding temperature $y_3 = T_{\mathrm{ew,le}}$, and the opposite-lead-end end-winding temperature $y_4 = T_{\mathrm{ew,ole}}$. For the derating algorithm, the loss of life function (2.25) is discretized

$$LF(y_i(\cdot),\, k) = \sum_{m=1}^{k} \frac{\tau_C}{L(y_{i,k})} \qquad i = 1, 3, 4 \tag{3.1}$$

with the MPC step size τ_C and evaluated individually for each output temperature.

For use in the optimization cost function, the discrete loss of life function is normalized by the desired lifetime L_d. This yields a relative measure of how much lifetime is lost during the time step k in the form

$$\lambda_{lt}(y_{i,k}) = \frac{L_d}{L(y_{i,k})}\ . \tag{3.2}$$

This measure allows systematic incorporation of the temporary overload capability of the motor into the design of the derating algorithm. During time periods where $\lambda_{lt}(y_{i,k}) > 1$, the winding isolation is deteriorating faster than permissible to achieve the desired lifetime L_d. It is possible to compensate periods with faster aging with periods where $\lambda_{lt}(y_{i,k}) < 1$.

To ensure that the actual lifetime of the PMSM windings achieves the desired lifetime, the temperatures $y_i(t)$, $i = 1, 3, 4$ must fulfill the condition

$$\frac{1}{N_{lt}} \sum_{k=1}^{N_{lt}} \lambda_{lt,k}(y_{i,k}) \leq 1 \qquad \text{for } i = 1, 3, 4 \tag{3.3}$$

with the number of steps in the desired lifetime $N_{lt} = \lceil \frac{L_d}{\tau_C} \rceil$.

The required lifetime of the PMSM is supposed to be at least 300 000 km or $L_d = 10\,000$ h [5]. It is possible to either directly choose the desired lifetime or derive it using equation (2.24)

$$L_d = L(T_d) \tag{3.4}$$

from a reference temperature T_d.

3.2 Estimation and Prediction

For the best utilization of the thermal durability of the motor by the derating algorithm, it needs to know the future vehicle state, desired speed trajectory, torque inputs, and external disturbances. Using the system model, the future state can be calculated, given the inputs and disturbances are known. However, especially with a human driver, whose commands cannot be predicted with certainty, the required quantities cannot be exactly known by the vehicle controller. To still be able to make useful derating decisions, a prediction model is used to provide estimates of future inputs and external disturbances.

There are several unknowns, including the vehicle, road, and external parameters. In the simple one-dimensional model (Section 2.6), the parameters are the vehicle mass, drag area and coefficient, rolling friction coefficient, and road slope. All of these can vary, e. g. different vehicle loading, a changing number of passengers, attachments to the car such as roof racks, and changing road conditions. Additionally, there can be influences on the vehicle which are not modeled in Section 2.6, e. g. wind. These extra model-plant mismatches can cause additional estimation errors.

To keep the focus on the derating algorithm, for this work, the vehicle mass, drag parameters, and rolling friction coefficient are assumed constant and known. This leaves the road slope γ as the only parameter of the mechanical vehicle model that has to be estimated. With the parameters known or estimated, the future desired input and vehicle state is predicted, which includes the vehicle speed and motor torque. In the following sections, the approaches to estimate the road slope and predict the future desired torque and speed are detailed.

3.2.1 Parameter Estimation

In Chapter 1, some estimation approaches found in the literature are referenced. The slope estimation is based on the longitudinal vehicle model (2.26). The quantities used for this estimation are the motor speed and torque. The motor speed is measured and the motor torque is calculated from the electrical quantities of the PMSM (Section 2.1). The slope estimation is implemented using an Extended Kalman Filter (EKF). The estimator

is evaluated using simulations. Additive Gaussian noise is added to the measured motor speed and the motor torque used by the EKF.

For the EKF, the discretized mechanical model is extended with a second state for the slope, which is assumed as quasi-constant. This gives

$$\begin{aligned} \mathbf{x}_{k+1} &= \begin{bmatrix} v_{k+1} \\ \gamma_{k+1} \end{bmatrix} = \mathbf{x}_k + t_s \begin{bmatrix} \frac{1}{m_{\text{eff}}}(F_{a,k} - F_{d,k} - F_{r,k} - F_{g,k}) \\ 0 \end{bmatrix} + \mathbf{w}_k \\ y_k &= \mathbf{c}^{\mathrm{T}} \mathbf{x}_k + v_k \end{aligned} \tag{3.5}$$

with the output vector $\mathbf{c}^{\mathrm{T}} = \begin{bmatrix} 1 & 0 \end{bmatrix}$ and additive process and measurement noise $\mathbf{w}_k$ and v_k, respectively. For the system (3.5), an extended Kalman filter is implemented [26] to estimate the road slope $\hat{\gamma}_k$.

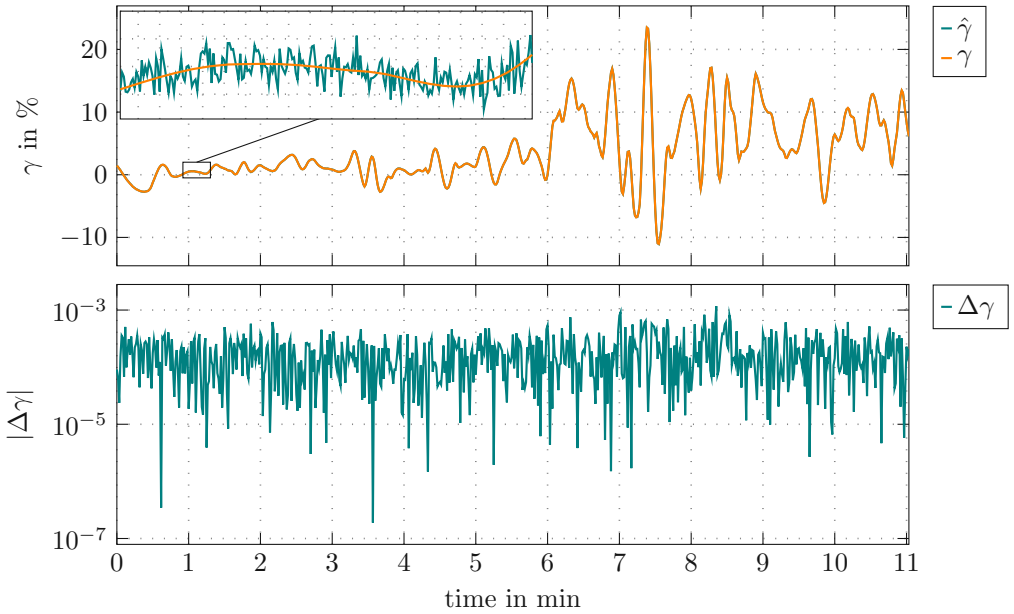

Figure 3.1: Simulation of slope estimation with additive Gaussian measurement noise for the motor speed and motor torque.

Figure 3.1 shows a simulation of the slope estimation using the EKF and the corresponding error $\Delta\gamma = \gamma - \hat{\gamma}$ for a simulated road with changing slope. The upper graph shows the true and estimated road slope and includes a zoomed part. The EKF estimates the slope with good accuracy despite the measurement noise. The lower graph shows the absolute estimation error $|\Delta\gamma|$ with a logarithmic scale.

3.2.2 Prediction

The next step is to use the estimated slope to predict the future desired motor torque and vehicle speed. As no future information concerning the slope is available, it is assumed to be constant within the prediction horizon. The goal is to get a more realistic prediction than that the current torque and motor speed stay constant within the prediction horizon.

The evolution of the speed is predicted within the prediction horizon using the mechanical model (2.26) and the currently desired motor torque and assuming that this torque stays constant in the predicted time span, except when limits are reached. These limits include the speed and torque limits in equation (2.4). Additionally, when decelerating, the lower speed limit is 0 m/s. This means braking will stop the vehicle but will not lead to negative speeds. If the vehicle accelerates in the prediction horizon, it may happen that the torque limit given in (2.4b) and thus also the predicted torque decrease. When the speed reaches one of its limits, the predicted torque is adapted so that the speed stays constant for the rest of the prediction interval.

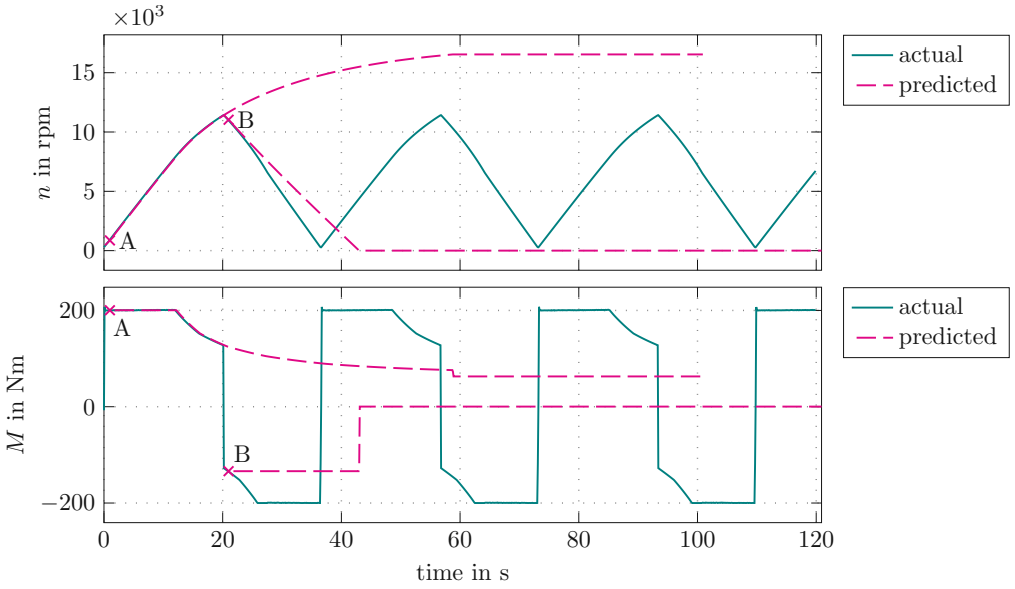

Figure 3.2: Scenario to show the prediction of torque and speed. The solid line shows the actual values and the dashed lines show the predicted values. Predictions from two starting points A and B are plotted.

Figure 3.2 shows an example prediction for a driving scenario with repeated acceleration and braking with zero slope ($\gamma = 0$). At point A, a high torque is used for acceleration. The prediction matches the actual torque and speed until the braking phase starts. The change from acceleration to braking cannot be predicted, and therefore the predicted speed continues to increase until the maximum speed is reached. The predicted torque starts with a constant value and then follows the torque limit. When the maximum speed is reached, the torque is reduced so that the remaining torque ensures a constant speed. At point B, the vehicle brakes and a speed decrease is predicted. The scenario simulates braking with the maximum available (negative) motor torque. The fact that the torque limit is relaxed because of the decreasing speed is not considered, i. e., the predicted torque stays constant and does not match the actual torque. This also results in a prediction error of the speed. When the speed reaches zero, the predicted torque is also set to zero.

This highlights a disadvantage of the implemented prediction approach: Future changes of the driving behavior cannot be anticipated, and only the currently available information

about the slope and desired torque is used. However, the proposed prediction approach is more accurate than the assumption of constant torque and speed and allows for less conservative decisions of the derating algorithm. This is especially true for driving maneuvers that utilize high torques, like overtaking. However, it does not predict the typical behavior of human drivers very well and does not account for the typically changing road slope. In [27], an approach using machine learning is used to improve the prediction of the control reference for model predictive control in vehicles. In the outlook of the current work (see Chapter 5), possible extensions are mentioned to include additional information for a better prediction of the slope as well as the torque and speed.

For comparison, the results of two additional torque and speed prediction approaches are shown in Chapter 4. The first is the assumption that the current speed n stays constant and that the torque equals the maximum torque $M_{\text{lim}}(|n|)$. This approach is used in [13] and can be used when no additional information, such as vehicle acceleration or road slope, is available to the vehicle controller. The second (admittedly unrealistic) prediction approach uses the desired speed and torque known from the test cycles in the simulation.

3.3 Static Derating Curves

Before the MPC-based derating algorithm is developed in the following sections, this section explains the derating approach using static curves. This traditional approach serves as a comparison in the simulation studies in Chapter 4. Individual derating factors $f_{i,\text{drt}}$ are calculated based on a number of quantities: temperature of the windings T_{Cu}, rotor T_{pm}, cooling water T_w, cooling oil T_{oil}, and flow rate of water Q_w and oil Q_{oil}. For every quantity, two thresholds $\vartheta_{i,1}$ and $\vartheta_{i,2}$ are defined. Using the saturation function

$$f_{i,\text{drt}} = \begin{cases} f_{i,\max} & \text{if} \quad \vartheta_i > \vartheta_{i,2} \\ f_{i,\min} & \text{if} \quad \vartheta_i < \vartheta_{i,1} \\ f_{i,\min} + (\vartheta_i - \vartheta_{i,1}) \frac{f_{i,\max} - f_{i,\min}}{\vartheta_{i,2} - \vartheta_{i,1}} & \text{otherwise} \end{cases}, \quad \text{for } \vartheta_i = T_{\text{Cu}}, T_{\text{pm}}, T_w, T_{\text{oil}}, Q_w, Q_{\text{oil}} \tag{3.6}$$

the respective derating curves are defined. Table 3.1 lists the parameters of the static derating curves. The final derating factor $f_{\text{drt}} \in [0,\, 1]$ is determined as the minimum of all component factors

$$f_{\text{drt}} = \min_i (f_{i,\text{drt}}) \tag{3.7}$$

and is used to limit the torque to the range $[-M_{\text{drt}},\, M_{\text{drt}}]$ with

$$M_{\text{drt}} = f_{\text{drt}} M_{\text{lim}}(|n|) \tag{3.8}$$

and $M_{\text{lim}}(|n|)$ from (2.4b). Hence, if the torque M_d is requested, the torque

$$M(M_d) = \begin{cases} M_{\text{drt}} & \text{if} \quad M_d > M_{\text{drt}} \\ -M_{\text{drt}} & \text{if} \quad M_d < -M_{\text{drt}} \\ M_d & \text{otherwise} \end{cases} \tag{3.9}$$

is actually applied.

Quantity	$\vartheta_{i,1}$	$\vartheta_{i,2}$	$f_{i,\min}$	$f_{i,\max}$
T_{Cu}	150 °C	170 °C	1	0
T_{pm}	120 °C	140 °C	1	0
T_w	70 °C	80 °C	1	0
T_{oil}	120 °C	135 °C	1	0
Q_w	0.5 l/min	1 l/min	0	1
Q_{oil}	0.5 l/min	1 l/min	0	1

Table 3.1: Parameters of the static derating curves.

3.4 Optimization Problem

This section presents the optimization problem underlying the MPC-based derating algorithm. The goal of the derating approach is to thermally protect the PMSM while still permitting high torques if they are requested.

Based on the desired torque M_d and the derating factor f_{drt}, the applied torque M is computed using (3.8) and (3.9). In the MPC-based derating algorithm, an optimization problem is repeatedly solved to find the trajectory of the optimal derating factor. The discrete-time OCP at the time step k is

$$\min_{\left(\widetilde{f}_{\mathrm{drt},l}\right)} \quad J\left(\mathbf{x}_{t,k},\, \left(\widetilde{f}_{\mathrm{drt},l}\right)\right) = \sum_{l=0}^{N-1} d_{k+l}\left(\widetilde{f}_{\mathrm{drt},l},\, \widetilde{\mathbf{x}}_{t,l+1}\right) \tag{3.10a}$$

$$\begin{aligned} \text{s.t.} \quad & \widetilde{\mathbf{x}}_{t,0} = \mathbf{x}_{t,k} \\ & \widetilde{\mathbf{x}}_{t,l+1} = \mathbf{F}_k\left(\widetilde{\mathbf{x}}_{t,l},\, \widetilde{f}_{\mathrm{drt},l},\, \left(\widetilde{M}_{d,l,j}\right),\, (\widetilde{n}_{l,j})\right) && \forall l \in [0,\, N-1] \\ & 0 \leq \widetilde{f}_{\mathrm{drt},l} \leq 1 && \forall l \in [0,\, N-1] \\ & \widetilde{\mathbf{y}}_l = \mathbf{C}\widetilde{\mathbf{x}}_{t,l} \leq \mathbf{T}_{\max} && \forall l \in [1,\, N] \end{aligned} \tag{3.10b}$$

with the prediction horizon length $N = 10$ and stage cost $d_{k+l}\left(\widetilde{f}_{\mathrm{drt},l},\, \widetilde{\mathbf{x}}_{t,l+1}\right)$. The variables $\widetilde{\mathbf{x}}_{t,l+1}$ and $\widetilde{f}_{\mathrm{drt},l}$ denote the predicted values of the state vector of the reduced-order model and the derating factor, respectively, at the time steps $k+l$ and $k+l+1$, respectively. The optimized derating factors are assembled in the sequence $\left(\widetilde{f}^{*}_{\mathrm{drt},l}\right)$. The predicted desired torque and speed trajectories $\left(\widetilde{M}_{d,l,j}\right)$ and $(\widetilde{n}_{l,j})$, respectively, are computed according to Section 3.2.2. The discrete-time dynamics $\mathbf{F}_k\left(\widetilde{\mathbf{x}}_{t,l},\, \widetilde{f}_{\mathrm{drt},l},\, \left(\widetilde{M}_{d,l,j}\right),\, (\widetilde{n}_{l,j})\right)$ are based on the discrete-time model from Section 2.7 and include the current setpoint calculation, the loss model, and the reduced-order temperature model. Algorithm 1 explains how the state trajectory is predicted in the OCP. For computational efficiency, the state matrix $\mathbf{A}_{r,k}$, heat flows to the cooling fluids $\mathbf{q}_k$, and thermal conductances $G_k(\mathbf{p}_{s,k},\, n_k)$ are only calculated once per prediction horizon and not updated while solving the OCP. The inputs of the algorithm are the previous state $\widetilde{\mathbf{x}}_{t,l}$, the derating factor $\widetilde{f}_{\mathrm{drt},l}$ to be optimized, and the predicted sequences of the desired motor torque $\left(\widetilde{M}_{d,l,j}\right)$ and motor speed $(\widetilde{n}_{l,j})$. The

model is discretized using a multi-step forward Euler method, with N_d intermediate time steps.

Algorithm 1 $\widetilde{\mathbf{x}}_{t,l+1} = \mathbf{F}_k\Big(\widetilde{\mathbf{x}}_{t,l},\ \widetilde{f}_{\mathrm{drt},l},\ \Big(\widetilde{M}_{d,l,j}\Big),\ (\widetilde{n}_{l,j})\Big)$

$\widetilde{\mathbf{x}}_{t,l,0} \leftarrow \widetilde{\mathbf{x}}_{t,l}$
$M_{\mathrm{drt},l} \leftarrow \widetilde{f}_{\mathrm{drt},l}\, M_{\mathrm{lim}}(|\widetilde{n}_{l,0}|)$ ▷ (3.8)
for $j = 0, \ldots, N_d - 1$ **do**
$\begin{bmatrix} T_{\mathrm{Cu},j} & T_{\mathrm{pm},j} & \ldots \end{bmatrix}^{\mathrm{T}} \leftarrow \mathbf{C}\,\widetilde{\mathbf{x}}_{t,l,j}$ ▷ (2.19b)
$M_j \leftarrow \begin{cases} M_{\mathrm{drt},l} & \text{if} \quad \widetilde{M}_{d,l,j} > M_{\mathrm{drt},l} \\ -M_{\mathrm{drt},l} & \text{if} \quad \widetilde{M}_{d,l,j} < -M_{\mathrm{drt},l} \\ \widetilde{M}_{d,l,j} & \text{otherwise} \end{cases}$ ▷ (3.9)
$\omega_{e,j} \leftarrow 2\pi\, \widetilde{n}_{l,j}\, p$
$\mathbf{i}_{s,j} \leftarrow \mathbf{f}_{\mathrm{ops}}(M_j,\ \omega_{e,j},\ T_{\mathrm{Cu},j},\ T_{\mathrm{pm},j})$ ▷ (2.33)
$\mathbf{u}_j \leftarrow \begin{bmatrix} \mathbf{i}_{s,j}^{\mathrm{T}} & n_j \end{bmatrix}^{\mathrm{T}}$
$\mathbf{g}_j \leftarrow \mathbf{g}(\mathbf{u}_j,\ \mathbf{C}_{r,\mathrm{avg}}\widetilde{\mathbf{x}}_{t,l,j})$
$\dot{\widetilde{\mathbf{x}}}_{t,l,j} \leftarrow \mathbf{A}_{r,k}\widetilde{\mathbf{x}}_{t,l,j} + \mathbf{B}_r \begin{bmatrix} \mathbf{q}_k^{\mathrm{T}} & \widetilde{\mathbf{g}}_j^{\mathrm{T}} \end{bmatrix}^{\mathrm{T}}$ ▷ (2.19a)
$\widetilde{\mathbf{x}}_{t,l,j+1} \leftarrow \widetilde{\mathbf{x}}_{t,l,j} + t_s \dot{\widetilde{\mathbf{x}}}_{t,l,j}$ ▷ Forward Euler Method
end for
$\widetilde{\mathbf{x}}_{t,l+1} \leftarrow \widetilde{\mathbf{x}}_{t,l,N_d}$

The output matrix $\mathbf{C}$ from (2.19b) gives the predicted temperatures that are limited by

$$\begin{aligned} \mathbf{T}_{\mathrm{max}} &= \begin{bmatrix} T_{\mathrm{max,Cu}} & T_{\mathrm{max,pm}} & T_{\mathrm{max,ew,le}} & T_{\mathrm{max,ew,ole}} \end{bmatrix} \\ &= \begin{bmatrix} 250\,^{\circ}\mathrm{C} & 140\,^{\circ}\mathrm{C} & 250\,^{\circ}\mathrm{C} & 250\,^{\circ}\mathrm{C} \end{bmatrix} . \end{aligned} \tag{3.11}$$

However, the stator temperatures never reach these hard limits in practice. The stator temperatures are additionally considered in the stage cost

$$d_{k+l}\Big(\widetilde{f}_{\mathrm{drt},l},\ \widetilde{\mathbf{x}}_{t,l+1}\Big) = -w_{u,l}\,\widetilde{f}_{\mathrm{drt},l} + k_{\mathrm{lt}}\frac{1}{3}\sum_{i=1,3,4}\lambda_{lt}(\widetilde{y}_{i,l+1}) \ . \tag{3.12}$$

It uses the weighting factor k_{lt} to balance between two components, i. e. the derating factor f_{drt} and the loss-of-life term $\lambda_{lt}(\widetilde{y}_{i,l+1})$ according to (3.2) evaluated for the active winding and the end-windings. The loss of life term has the effect that for high temperatures, the cost strongly increases.

In the stage cost, the derating factor has a negative sign, which means that higher allowed motor torques decrease the cost. It is weighted with the factor

$$w_{u,l} = \frac{1 - k_w}{N} + k_w\,\frac{2(N - 1 - l) + 1}{N^2} \ , \tag{3.13}$$

which depends on l and the user-defined tuning factor $k_w \in [0, 1]$. The factor k_w controls how much stronger derating factors are weighted early in the prediction horizon. For

$k_w = 0$, uniform weighting is achieved. For $k_w > 0$, $w_{u,l}$ decreases linearly with l. The non-uniform weighting is motivated by the physical properties of the mechanical vehicle model (see Section 2.6). A detailed explanation and derivation of (3.13) can be found in Appendix A.1. Non-uniform weighting results in an increase of the immediate torque responsiveness and makes the derating algorithm less conservative.

In the derating algorithm by Wallscheid and Böcker [11], the cost function weights the track completion time. The algorithm by Winkler et al. [12] weights the speed error. These strategies are not directly usable in the developed derating algorithm because the mechanical vehicle model state is not part of the MPC scheme. Therefore, the cost function (3.10a) weights the derating factor which indirectly has an influence on the vehicle speed, as discussed in Appendix A.1.

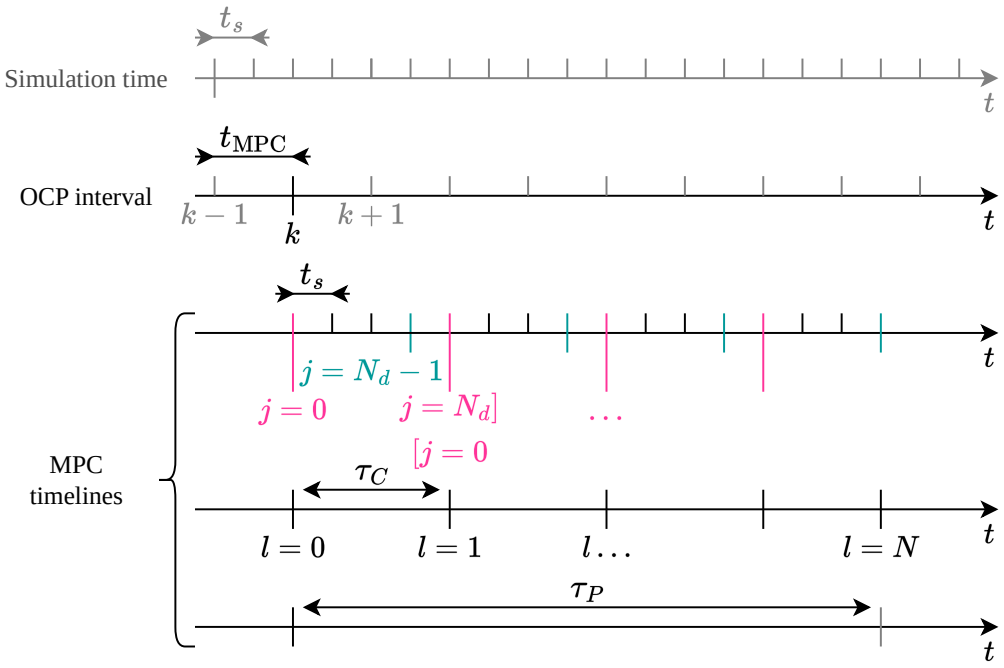

Figure 3.3: Timeline and time constants in the MPC.

Figure 3.3 shows the timelines and time intervals used in the MPC-based derating algorithm. The first timeline is associated with the simulation, which uses a sample time $t_s = 0.1\,\mathrm{s}$. The OCP is solved at every time step k. In the time interval between these steps, the optimal derating factor f^*_{drt} and torque limit M_{drt} stays constant. The length of this interval t_{MPC} determines how much time is available for solving the OCP. The timeline with the index $j = 0, \ldots, N_d$ is associated with the multi-step forward Euler method using the sample time t_s. The index j refers to the intermediate time instant j between the major grid points l and $l+1$ on the timeline of the optimization problem (3.10). This timeline has $N+1$ steps of size τ_C. In the OCP, the derating factors $\left(\widetilde{f}_{\mathrm{drt},l}\right)$ for $l = 0, \ldots, N-1$ stay constant for the interval τ_C, which is the step size for input parametrization. The last timescale shows the prediction horizon $\tau_P = N\tau_C$.

3.5 Solving the Optimization Problem

In this work, the OCP is solved as follows. The discrete-time motor model is evaluated as explained in Algorithm 1. The OCP only uses the state $\mathbf{x}_{t,k}$ of the reduced thermal model (cf. Section 2.4.2) and does not include the mechanical vehicle model (Section 2.6). However, the vehicle model is implicitly considered via the prediction of the future motor torque and speed.

The implementation of the nonlinear optimization problem is done using the nlmpc library of MATLAB. Internally, it uses full discretization of the OCP and solves the optimization problem using the fmincon function. The optimal solution is computed with the interior-point method. Additionally, warm start is implemented to use the previous solution to initialize the optimization variables. A good initial guess of the optimization variables can speed up convergence, i. e. fewer iterations are required to find the optimal solution.

3.6 MPC-Based Derating

This section presents the MPC-based derating algorithm, which uses the slope estimation (Section 3.2.1), motor torque and speed prediction (Section 3.2.2), and the optimization problem from Section 3.4.

At each time step k, the derating controller estimates the road slope $\hat{\gamma}$, predicts the future desired motor torque and speed, and computes all prerequisites for the optimization problem. These prerequisites include evaluating $\mathbf{A}_{r,k}$ and $\mathbf{q}_k$ from the motor speed n and the cooling inputs $\mathbf{p}_{s,k}$ (see Section 2.7). The optimization problem is the centerpiece of the MPC-based derating algorithm. Its solution is the optimal sequence of future derating factors $\left(\widetilde{f}^*_{\mathrm{drt}}\right)$. The derating algorithm sets the torque limit

$$M_{\mathrm{drt},k} = f_{\mathrm{drt},k} M_{\mathrm{lim}}(|n_k|) \ , \tag{3.14}$$

according to (3.8) using the optimal derating factor $f_{\mathrm{drt},k} = \widetilde{f}^*_{\mathrm{drt},0}$ at the time step $l = 0$ of the optimization horizon.

The cost function (3.10a) combines both objectives, maximizing the derating factor f_{drt} and reducing thermal aging of the stator windings. Because the MPC problem does not have the form of a tracking problem, it belongs to the class of economic MPC [10].

In [10], methods to formally prove stability and proper performance are presented. However, due to the complexity of the problem and the used models, no mathematical proof of stability or performance is performed in this work. The developed algorithm is validated using simulation studies in Chapter 4.

Figure 3.4 shows a visualization of active winding temperature trajectories obtained with the MPC. It shows the time intervals $t_{\mathrm{MPC}} = 0.1\,\mathrm{s}$, $\tau_C = 10\,\mathrm{s}$, and $\tau_P = 100\,\mathrm{s}$ explained in Section 3.4. This implementation differs from the usual discrete-time MPC formulation, in which the control horizon is both, the step size for input parametrization (τ_C), and the time period t_{MPC} after which the optimization problem is solved again. This approach allows to reduce the number of optimization variables (and therefore computation time) and to still compute a new derating factor f_{drt} when the vehicle state and inputs, i. e. speed

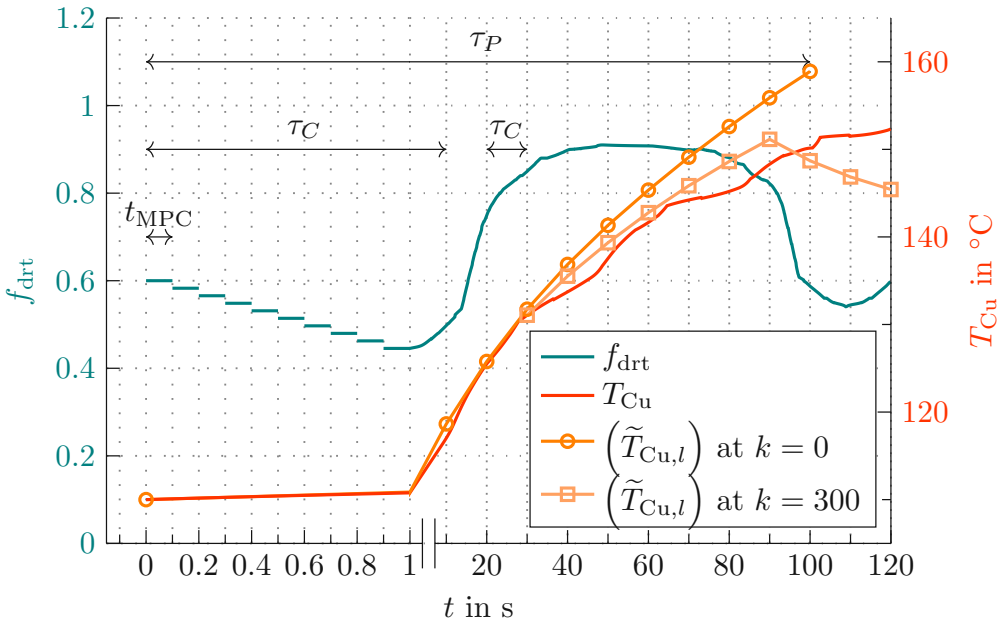

Figure 3.4: Timeline and time parameters in the MPC. The time axis is non-uniformly scaled to show t_{MPC}, τ_C, and τ_P. The derating factor f_{drt} as well as the copper temperature T_{Cu} and its prediction $\left(\widetilde{T}_{\mathrm{Cu},j}\right)$ at two selected MPC steps ($k = 0$ at $t = 0s$, and $k = 300$ at $t = 30s$) are plotted.

and torque, change. As discussed in Section 2.7, the MPC uses a performance-optimized thermal model that neglects the changing cooling parameters $\mathbf{p}_s$ in the prediction horizon. By calculating the derating factor f_{drt} after each time step t_{MPC}, the values of $\mathbf{p}_s$ are frequently updated.

For the simulation studies (presented in Chapter 4), $t_{\mathrm{MPC}} = t_s = 0.1\,\mathrm{s}$ is used. With this choice, the MPC-based derating algorithm does not achieve real-time performance on the used hardware (PC with Intel i5-8250U CPU, 16 GB RAM). The required CPU time is around 30 times longer than the simulated time duration. Real-time performance (on the used hardware) can be achieved by choosing $t_{\mathrm{MPC}} = 30t_s = 3\,\mathrm{s}$. The majority of the computation time is taken by the derating algorithm. The simulation model introduces only a small overhead.

3.7 Summary

Using the MPC-based derating algorithm with the time interval t_{MPC}, an optimal value for the derating factor f_{drt} is determined by solving the optimization problem (3.10). Its cost function considers the derating factor and thermal aging of the stator windings. Constraints are used to limit the permanent magnet temperature (Section 3.4). To obtain results that better utilize the thermal limits of the PMSM, the future desired torque and speed are predicted based on an estimation of the current road slope from an EKF.

Due to limited computational power, the MPC uses a simplified model of the PMSM, which does not include the mechanical vehicle model. This design decision leads to some limitations in defining the cost function compared to the derating approaches [11] and [12]. This decision is further discussed in Chapter 5, which also contains suggestions to minimize the disadvantages.

4 Evaluation and Results

In this chapter, simulations and evaluations of the developed derating algorithm are presented. The different approaches are compared based on simulation results including quantitative metrics. Additionally, studies of how tuning the parameters influences these results are conducted.

4.1 Simulation Setup

The derating approaches presented in Chapter 3 are evaluated and compared using different simulation studies. For the simulation it is assumed that the MPC-based derating algorithm has exact knowledge of the state of the reduced-order model, i. e. no observer for state estimation is used. In the simulation, the desired motor torque and motor speed are specified. This is done using test cycles that define a trajectory for torque and speed. Two different approaches are used to specify these trajectories.

The first one resembles a machine test bed, which directly controls the motor speed and defines the desired torque at each time step. This allows simulations that test specific scenarios (any combinations of torque and speed) without considering the vehicle dynamics which couple torque and speed.

The second approach simulates driving on a road, where the desired speed and road slope are specified and the mechanical model of the vehicle is used to determine the resulting vehicle and motor speed from the applied torque. In this case, the desired motor torque is determined using a driver model. A simple driver model in the form of a speed controller is used. It inverts the mechanical model (Section 2.6) to calculate the necessary torque to match the speed setpoint. Other ways to determine the torque setpoint from the desired speed would also be possible, such as more sophisticated speed controllers or simulating human behavior. Some of these approaches will be discussed in Chapter 5. However, to keep the focus on the derating algorithm, they are not used in the simulation studies.

The desired speed v_d and road slope γ are simulated in two scenarios: The first one is a simulated road where v_d and γ depend on the current position of the vehicle. For the second scenario, v_d and γ are parameterized as functions of the time. While the first scenario is useful to simulate undisturbed driving without stops on a road or racetrack, the second scenario allows to simulate traffic with stop-and-go driving or waiting at traffic stops.

The motor temperature is initialized to be homogenous at the value 110 °C. This temperature is chosen because it is below the temperature at which the static derating curves start limiting the torque (see Table 3.1). At the same time, it is relatively high to reduce the necessary simulation time until the temperature limits are actually approached. In practice, such an initial state could be the result of extended periods of highway driving.

Figure 4.1 shows the simulation setup for the case including the mechanical vehicle model. The following tasks are repeated for every time step. The desired speed trajectory is defined by the test cycle from which the speed controller derives the desired torque. The current speed v and state vector $\mathbf{x}_t$ of the reduced thermal model constitute the available state information for the controller. Using this information, the derating algorithm determines a derating factor and the maximum allowed motor torque M_{drt} according to equation (3.9), as explained in Section 3.4.

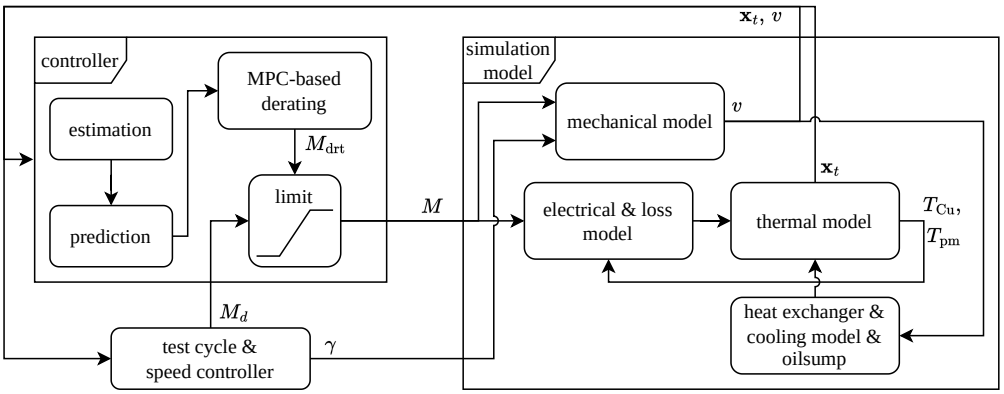

Figure 4.1: Simulation setup including the models from Chapter 2, test cycle, and vehicle controller for derating.

4.2 Test Cycles

The test cycles are designed so that the motor temperatures quickly rise to values where derating is necessary. This means that the test cycles demand high loads of the motor, often higher than usually expected in real driving situations.

In the electric motor, a high torque demand leads to high losses in the stator windings, which increases their temperatures. The rotor temperature typically increases during periods with high motor speeds due to increased eddy current losses and heat transfer from the stator. However, because the motor directly drives the oil pump (Section 2.3), there is a higher oil flow rate for cooling at higher motor speeds. The selected four test cycles include scenarios with both low and high speed and acceleration to simulate a variety of operating conditions.

The first test cycle shown in Figure 4.2a is a test bed simulation with constant motor speed and constant desired torque with a cycle length of 700 s. A constant speed of $n = 8000\,\text{rpm}$ (about half the maximum motor speed) is used. The desired torque is $M_d = 178\,\text{Nm}$, which is 90 % of the peak torque at the given motor speed. This combination of speed and torque presents a high load to the motor. Using the vehicle parameters to calculate the equivalent road parameters, the first load scenario corresponds to a vehicle speed of $v = 28.3\,\text{m/s} = 102\,\text{km/h}$ at a road slope of $\gamma = 22\,\%$.

The second cycle is defined in Figure 4.2b based on the desired vehicle speed and road slope. This scenario resembles a high-speed test cycle with the desired top speed

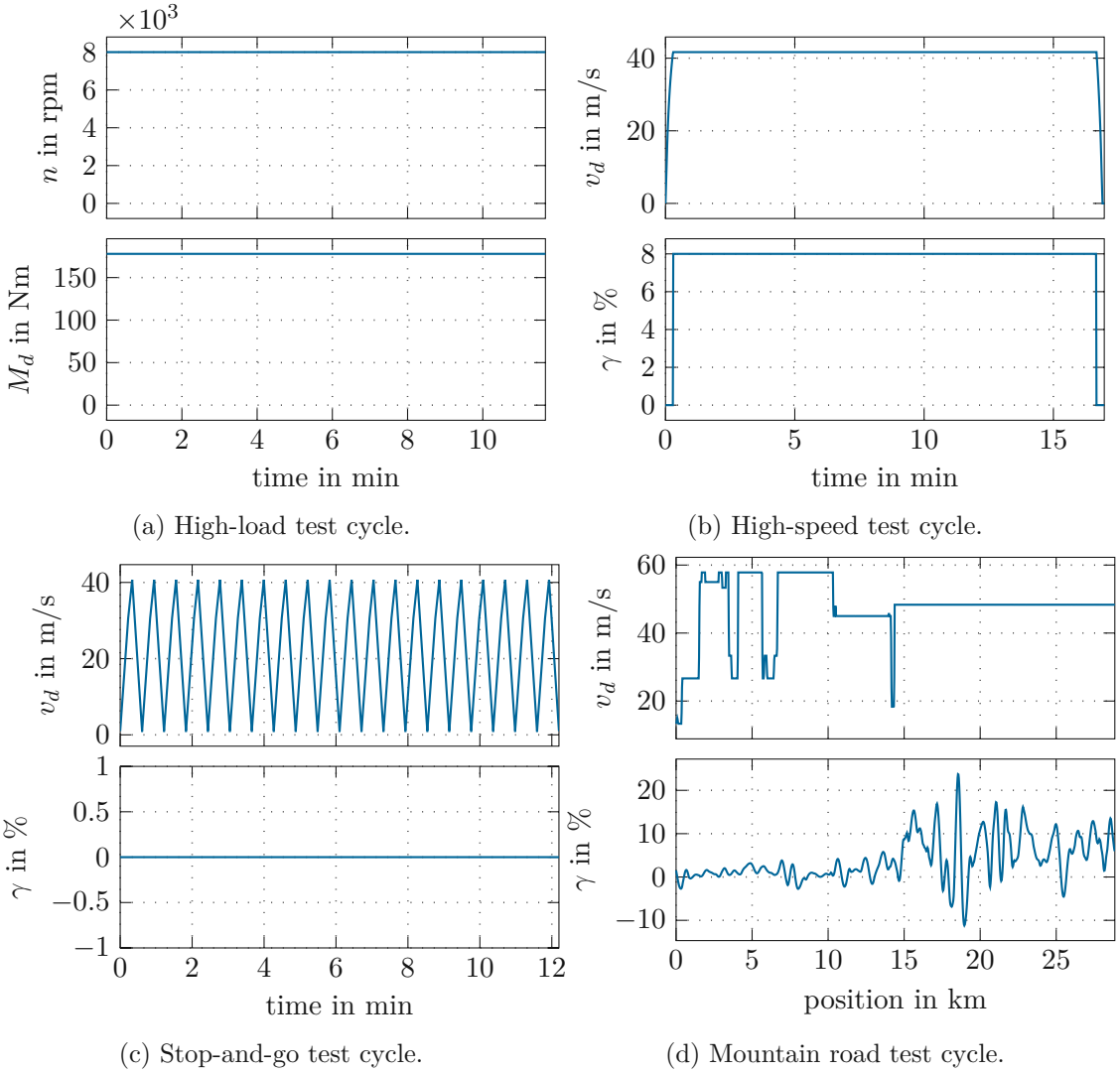

(a) High-load test cycle.

(b) High-speed test cycle.

(c) Stop-and-go test cycle.

(d) Mountain road test cycle.

Figure 4.2: Test cycles.

$v_d = 150\,\mathrm{km/h} = 41.7\,\mathrm{m/s}$, corresponding to a desired motor speed of $n_d = 11\,797\,\mathrm{rpm}$. The scenario also includes acceleration and braking phases at the start and the end so that the desired velocity starts and ends at zero. To increase the motor load, there is a constant road slope of $\gamma = 8\,\%$ during the phase of constant speed.

The third test cycle shown in Figure 4.2c represents an archetypical case of urban stop-and-go traffic. The desired velocity starts at zero and accelerates for 20 s, after which the maximum speed of the cycle is reached. Then, the vehicle is decelerated to zero velocity. This process is repeated 20 times during the scenario, which takes a total of 732 s. The road slope is zero in this cycle.

The last test cycle shown in Figure 4.2d was generated using road map data from a mountain road. To increase the load, the three-fold road speed limits are used as the desired velocity (limited to below the maximum vehicle speed). The slope starts with low

values in the first half of the road and has larger values and larger changes in the second half. The total road length is 28.9 km.

4.3 Simulations

In this section, the simulation results for each test cycle are presented, compared, and interpreted. Additionally, parameter studies to show the effect of the prediction horizon length τ_P, the weight distribution factor k_w in (3.13), and the desired lifetime L_d in (3.2) are conducted.

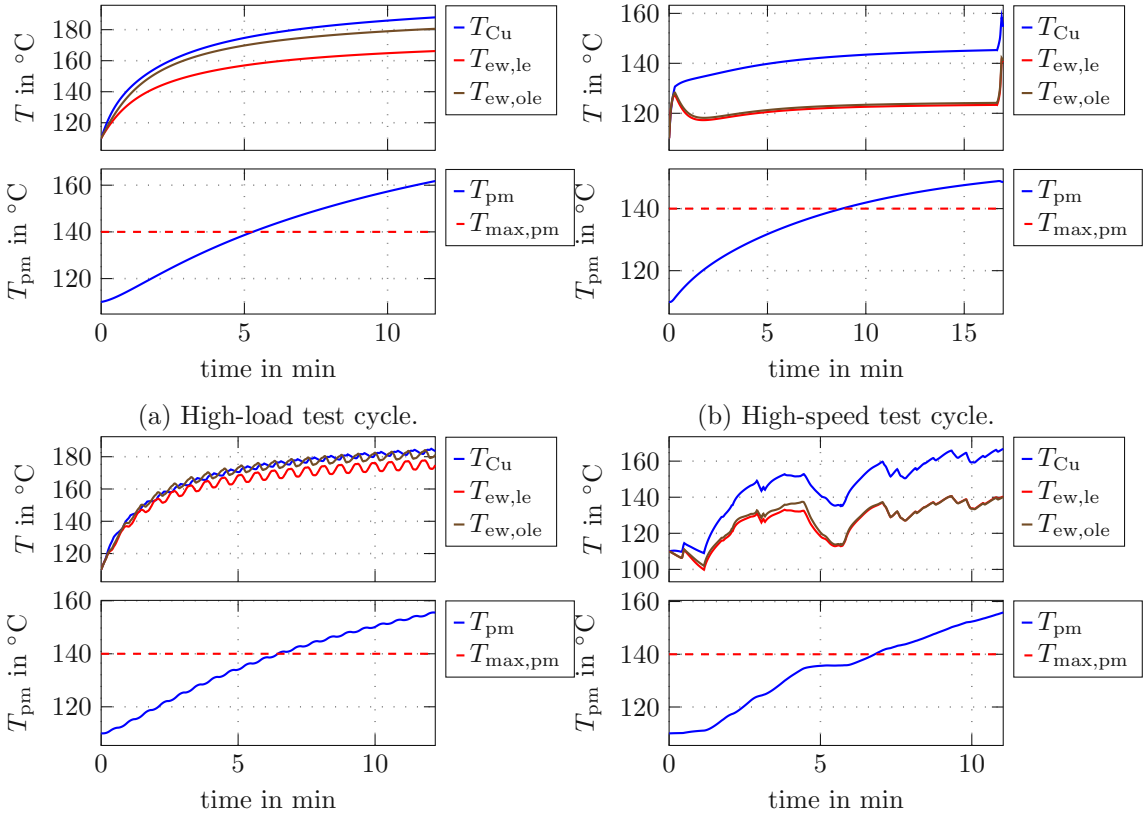

(a) High-load test cycle.

(b) High-speed test cycle.

(c) Stop-and-go test cycle.

(d) Mountain road test cycle.

Figure 4.3: Simulations without derating.

For each test cycle, temperature profiles without derating are shown in Figure 4.3. The three stator temperatures of the active windings T_{Cu}, lead-end end-windings $T_{ew,le}$, and opposing-lead-end end-windings $T_{ew,ole}$ are shown on one axis and the permanent magnet temperature T_{pm} on another axis. These results demonstrate that high temperatures above the limits would be reached when the torque is not limited. For the MPC-based derating, the stator temperatures y_i, $i = 1, 3, 4$ are weighted in the cost function by the loss of life term, i. e., the last term in (3.12). The limit $T_{max,pm} = 140\,°C$ for the permanent magnet temperature is also shown in Figure 4.3.

To distinguish between which prediction method from Section 3.2.2 is used in the MPC-based derating algorithm, the methods are identified using the following labels. *MPC 1)* is used to refer to the prediction method, explained in Section 3.2.2, which uses the mechanical model to predict the trajectories of the motor speed and torque. The assumption that the future motor speed and torque stay constant is designated as *MPC 2)*. The (unrealistic) method to use the known motor speed and torque from the simulated test cycle is referred to as *MPC 3)*.

The following sections present simulation results which show the behavior of the different derating approaches.

4.3.1 Static Curves and MPC-Based Derating Algorithm

First, the differences between the MPC-based derating algorithm and the derating using static curves are analyzed. For this purpose, the high-load test cycle (Figure 4.2a) is used. The corresponding simulated temperature profile without derating is shown in Figure 4.3a.

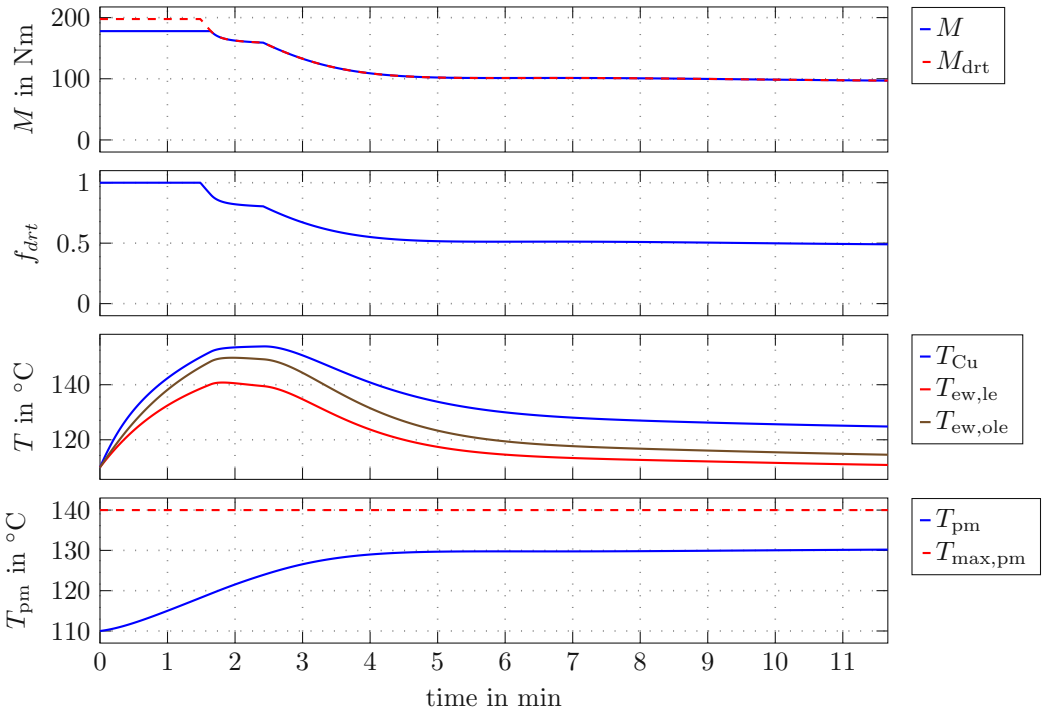

Figure 4.4: Simulation of the high-load test cycle with derating using static curves.

The subsequent plots including Figure 4.4 consist of several subplots showing relevant information about the derating. The first subplot shows the applied motor torque and the torque limit according to (3.9) and (3.10). The desired torque is limited to get the applied torque as described in Section 3.4. The second subplot shows the derating factor from (3.8). The last two subplots show the relevant motor temperatures.

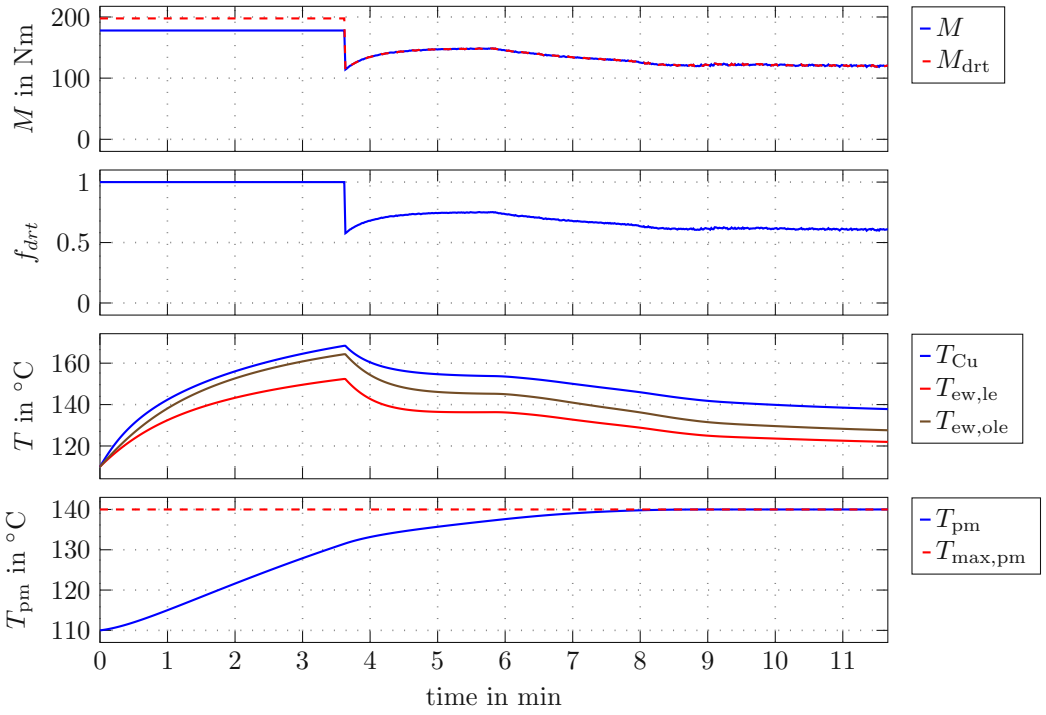

Figure 4.5: Simulation of the high-load test cycle with MPC-based derating *MPC 1)*.

Figure 4.4 shows the results for derating using static curves (Section 3.3). The plot of the motor speed is omitted because it stays constant in this test cycle. In this scenario, the derating factor starts at one and is reduced as soon as the copper temperature T_{Cu} reaches the lower threshold 150 °C. The derating factor continuously decreases, mainly because of other quantities such as the magnet temperature T_{pm} reaching their thresholds, until it settles at a stationary value of approximately $f_{\mathrm{drt}} = 0.50$.

Figure 4.4 shows the behavior that is typical for cycles with high desired torque, which also causes higher electromagnetic losses. Due to the high losses in the stator windings, their temperatures quickly rise. The permanent magnet temperature increases at a lower rate, heated by the other parts of the motor and the rotor losses, e. g. due to eddy currents.

Figure 4.5 shows the simulation results using MPC-based derating *MPC 1)*. Compared to derating using static curves, the derating factor stays at one for a longer time until there is a sudden drop at 3.6 minutes. The drop occurs when the predicted permanent magnet temperature reaches its limit within the prediction horizon. This causes the stator temperatures to stop increasing and slows the rate at which the magnet temperature rises to ensure that the constraint is not violated. The main benefit of the MPC-based derating algorithm is that it is possible to use the whole admissible temperature range up to the specified limits. The derating factor reaches a stationary value of $f_{\mathrm{drt}} = 0.60$, which is higher than with the static derating curve approach because the temperature limit of the permanent magnet is fully utilized. This shows that even for simple operating conditions with constant motor speed and constant desired torque, for which the static curves can be tuned best, the MPC-based derating satisfies the temperature limits while being less

restrictive on the available torque.

The next section examines the influence of the prediction of motor torque and speed in the prediction horizon on the MPC-based derating algorithm.

4.3.2 Prediction of Motor Speed and Torque

The MPC-based derating algorithm *MPC 1)* predicts the motor speed and torque trajectory during the prediction horizon, using the mechanical model as described in Section 3.2.2. This method is compared to *MPC 2)* which uses the assumption that the motor speed and torque stay constant and to *MPC 3)* which predicts the future based on the known trajectories of speed and torque from the test cycle. These comparisons use the high-speed test cycle (Figure 4.2b) and stop-and-go test cycle (Figure 4.2c) for which the temperature simulations without derating are shown in Figures 4.3b and 4.3c, respectively.

For the high-speed test cycle, the desired speed is constant for the majority of the time, which makes it easy to predict. The assumption used in *MPC 2)* that the motor speed and torque are constant, is reasonable for the high-speed test cycle except in the acceleration and braking phases.

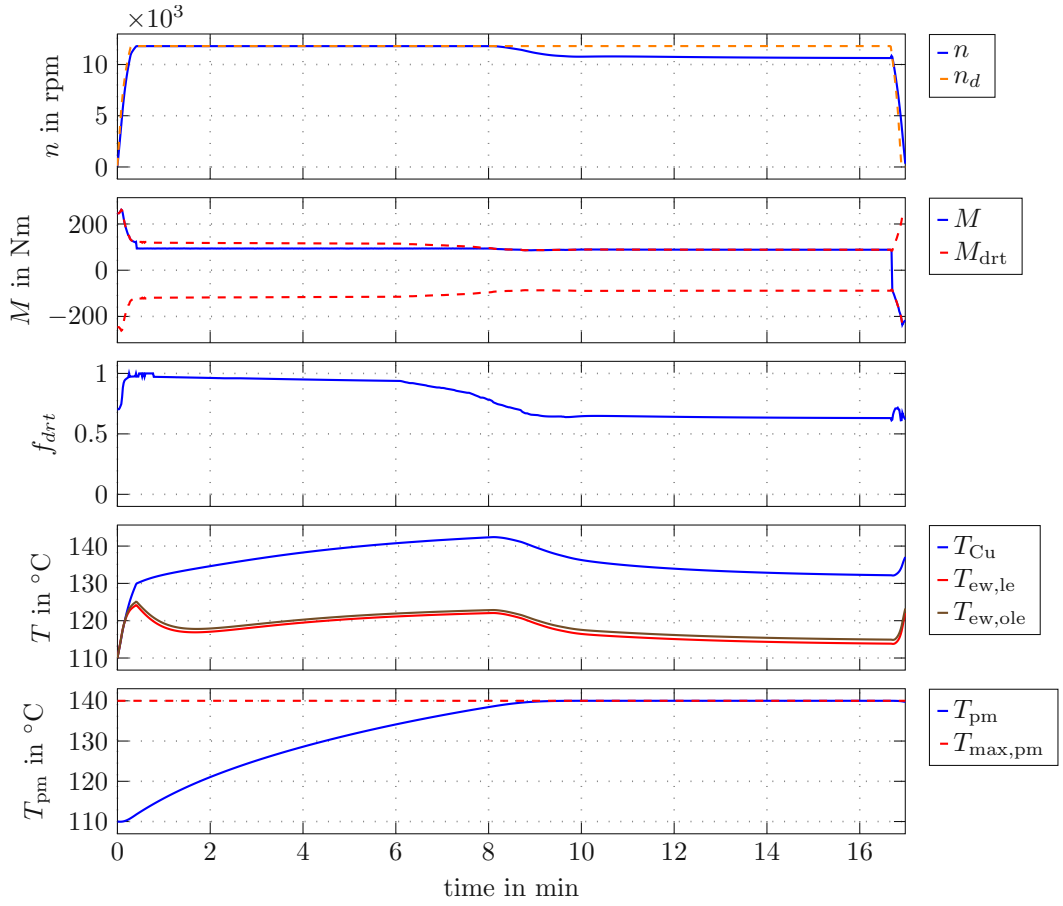

Figure 4.6: Simulation of the high-speed test cycle with MPC-based derating *MPC 2)*.

Figure 4.6 shows simulation results for the high-speed test cycle using MPC-based derating *MPC 2)*. At the beginning of the simulation, the derating factor starts with $f_{\text{drt}} = 0.7$ and increases to one after the acceleration phase. The lower derating factor at the beginning is due to the deviation between the predicted and real motor speed. According to the prediction, the motor speed stays lower, which also means that the oil pump has a lower oil flow rate and therefore a lower cooling capacity. At the same time, a high torque is predicted, which would cause the motor temperatures to quickly rise within the prediction horizon. Therefore, derating is applied even though the actual motor temperatures are far away from their limits. Later, the permanent magnet temperature rises and the derating factor is gradually reduced to a stationary value of about $f_{\text{drt}} = 0.64$. This ensures that the permanent magnet temperature stays within its limits.

The simulation result using method *MPC 1)* is shown in Figure 4.7. At the start, i. e., during the acceleration phase, no derating is applied and the derating factor stays at one because the increase of the motor speed is predicted. Between seven and eight minutes, the derating factor drops suddenly. This drop ensures that the permanent magnet temperature does not rise above its limit.

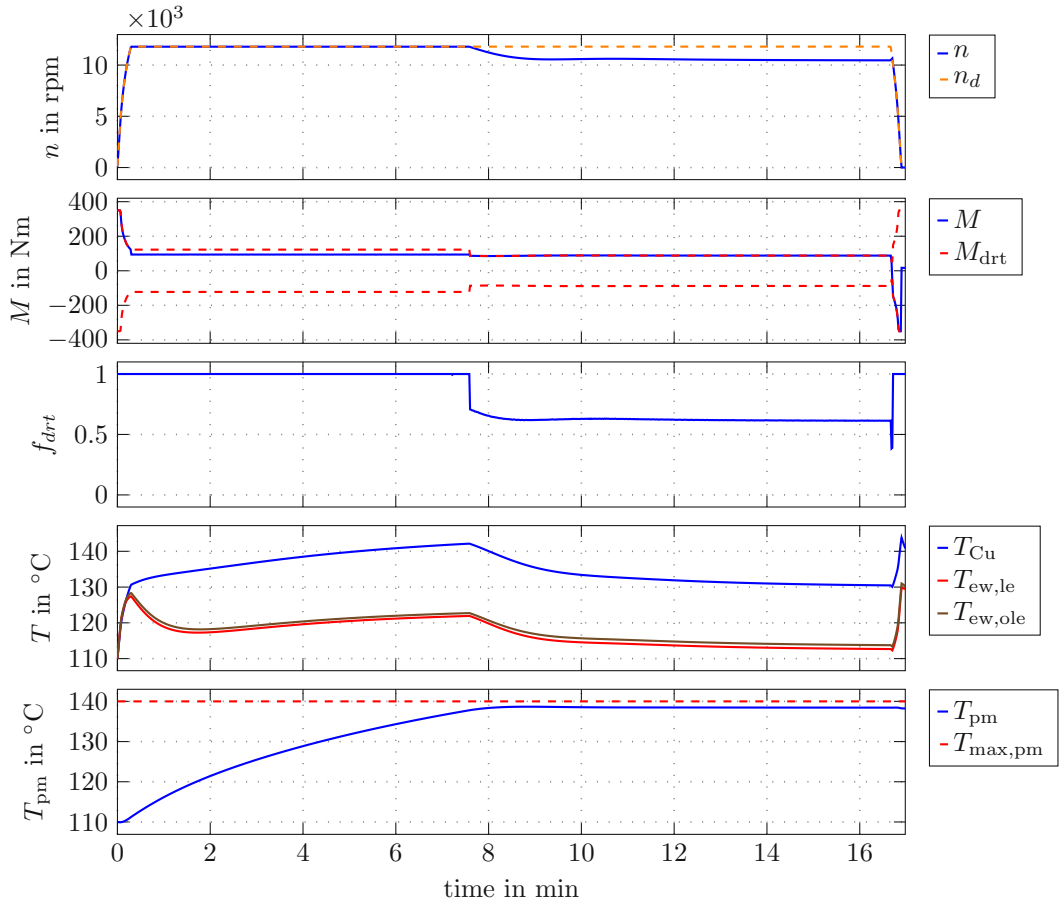

Figure 4.7: Simulation of the high-speed test cycle with MPC-based derating *MPC 1)*.

Another difference to the simulation result using *MPC 2)* is that the permanent magnet temperature stays approximately 1.5 °C below its limit because the stationary value of the derating factor $f_{\text{drt}} = 0.614$ is lower than in the simulation using *MPC 2)*. This is due to two factors. One is the time-dependent weighting of the derating factors in the cost function. In the optimization problem, the optimal solution can cause the derating factor at the current time to be slightly lower so that the derating factors at subsequent time steps do not have to be reduced as much. This effect will be investigated in Section 4.3.3 in a parameter study. However, this effect applies to both methods *MPC 1)* and *MPC 2)* and can only explain why the temperature stays below the limit and cannot explain the difference.

The second reason is caused by the prediction method used in *MPC 1)*. As explained in Section 3.2.2, the prediction is based on the desired torque without derating. Therefore, the actual motor speed stays lower than the prediction. However, the MPC-based derating takes into account the higher predicted motor speed, which would cause the temperatures to rise faster, and reduces the derating factor and torque more than necessary.

Known Future

The goal of the model-based prediction of desired motor torque and speed is to provide reliable information about the future load scenario, for the MPC-based derating algorithm. The best possible prediction would be to exactly know the desired inputs in the future. Therefore, the model-based prediction (*MPC 1)*) is compared to the (unrealistic) case where the future desired torque and speed are exactly known (*MPC 3)*).

For this comparison, the stop-and-go test cycle is used, for which the prediction accuracy varies a lot more than for the high-speed test cycle. Clearly, for this test cycle, the assumption in *MPC 2)* of constant speed and torque is not applicable and results in a bad prediction. The mechanical model-based prediction is more accurate, however, only until the next switch between acceleration and deceleration, as shown in Figure 3.2. The prediction errors result in an alternating over- and underestimation of the electrical losses in the later parts of the prediction horizon.

Figure 4.8 shows the simulation of the stop-and-go test cycle with MPC-based derating and the model-based prediction (*MPC 1)*). The first six acceleration and braking phases are performed without any derating ($f_{\text{drt}} = 1$). However, the motor temperatures, especially the stator temperature, quickly rise and the derating factor is reduced. The reduction happens during the acceleration phase in which a high load is predicted. This results in a bad speed tracking performance, i. e., the speed can no longer follow the desired trajectory.

The simulation results for the stop-and-go test cycle with MPC-based derating with exactly known future desired torque and speed (*MPC 3)*) are shown in Figure 4.9. The observed behavior is very different from the previous simulation results. The derating factor is reduced earlier than in Figure 4.8 but does not have to be reduced as much. Because the exact future of the desired speed and torque is known, the derating algorithm can better consider the torque demand after changes between acceleration and braking.

In comparison, this means that the model-based prediction results in less conservative derating in the short-term. With a known future, or when assuming constant speed and torque, the derating is more conservative, i. e. trades off short-term lower torque for

a higher derating factor in the long run. Therefore, using the model-based prediction, the speed tracking is better at the start of the test cycle but deteriorates when the motor temperatures approach their limits (Figure 4.8). Overall, the other two prediction approaches result in a lower speed tracking error.

In the next section, the influence of important tuning parameters of the MPC-based derating algorithm is investigated.

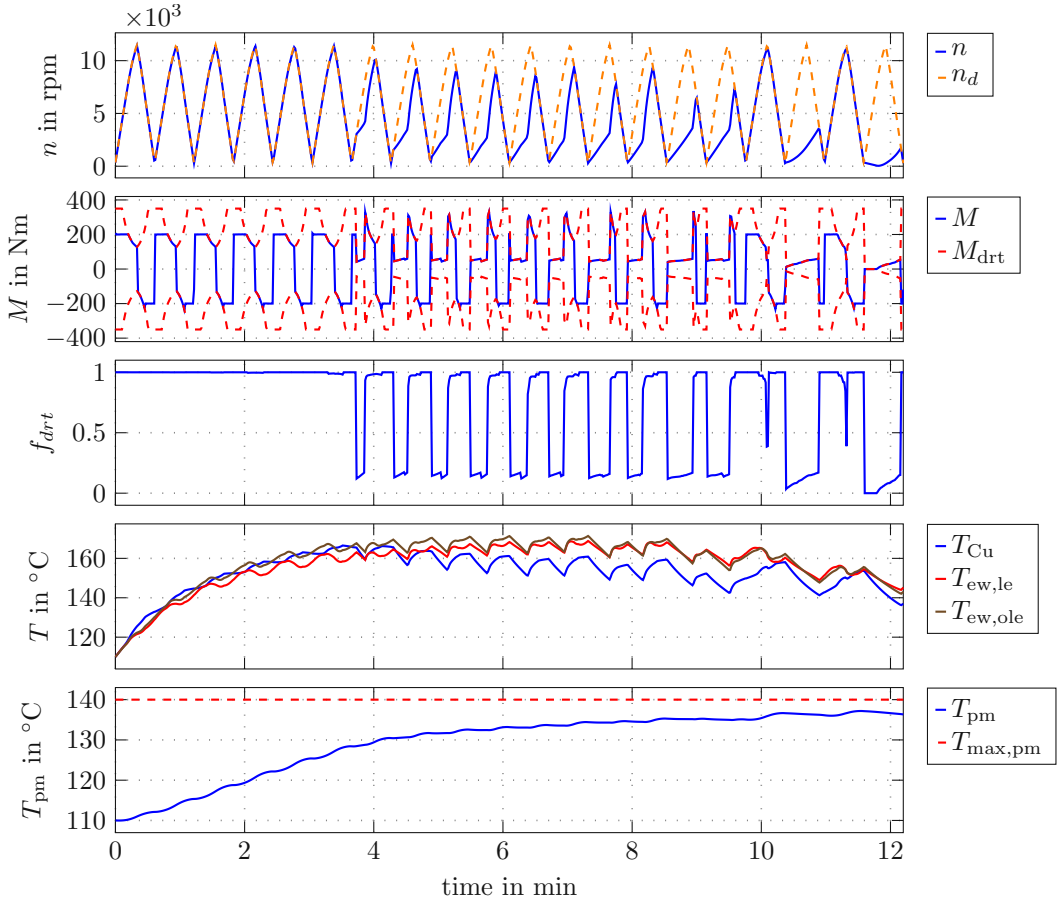

Figure 4.8: Simulation of the stop-and-go test cycle with MPC-based derating *MPC 1)*.

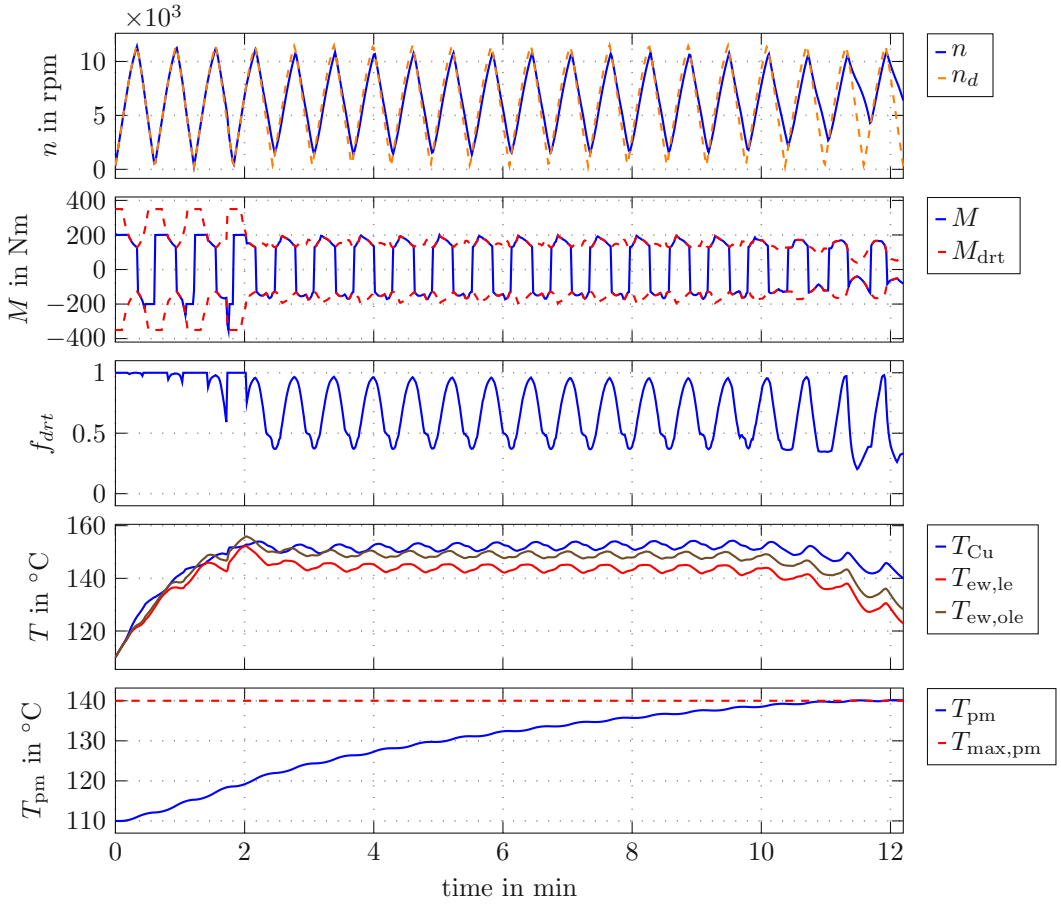

Figure 4.9: Simulation of the stop-and-go test cycle with MPC-based derating *MPC 3)*.

4.3.3 MPC Parameters

The analyzed parameters of the MPC-based derating algorithm are the prediction horizon length τ_P, weight distribution factor k_w in (3.13), and the desired lifetime L_d in (3.2), which modifies the temperature-dependent loss-of-life term in the cost function.

Prediction Horizon Length

As discussed in Section 3.4, the prediction horizon length is chosen long enough so that the temperature constraints can be satisfied and not too long so that the computation time is still reasonable. Figure 4.10 shows the simulation results of the high-load test cycle with MPC-based derating using *MPC 1)* and a reduced prediction horizon length of $\tau_P = 10\,\mathrm{s}$. This value is at the margin of being long enough and the simulated permanent magnet temperature slightly violates its limit between five and six minutes. If the optimization does not find an admissible solution, the derating factor and torque are set to zero. For even shorter prediction horizon lengths, the permanent magnet temperature limit would be considerably violated. Compared to the simulations with sufficiently long horizon

lengths (like Figure 4.5 with $\tau_P = 100\,\mathrm{s}$) a higher derating factor is computed and more torque is allowed. As a result, the temperature limits cannot be enforced and an undesired sudden reduction of the torque to zero occurs.

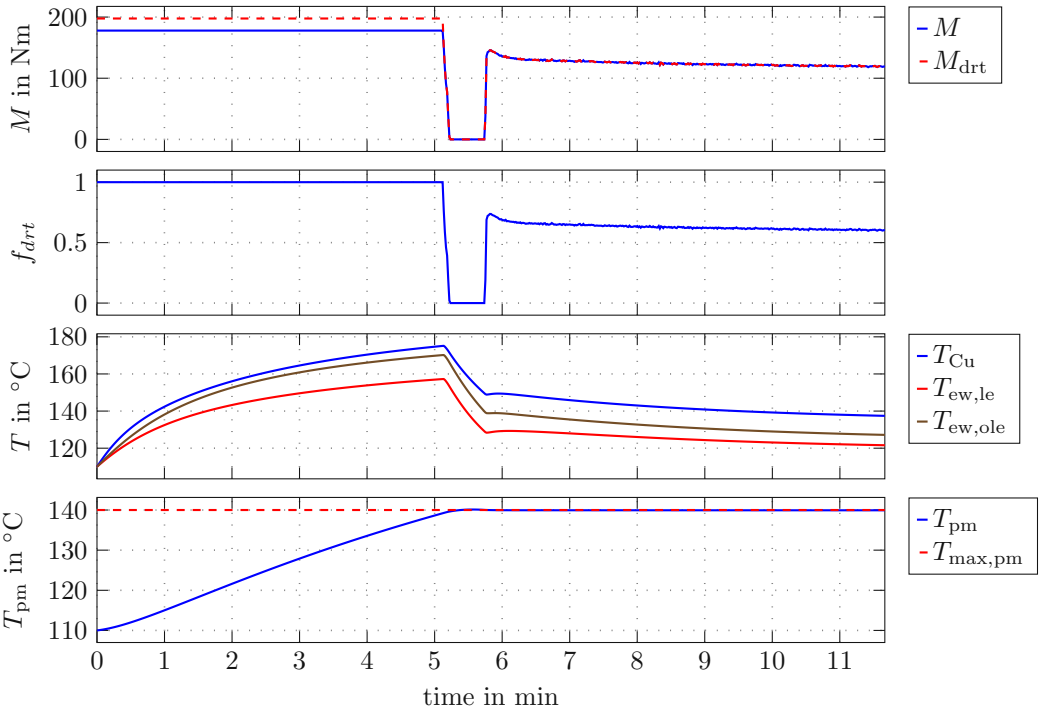

Figure 4.10: Simulation of the high-load test cycle with MPC-based derating *MPC 1)* with reduced prediction horizon length $\tau_P = 10\,\mathrm{s}$.

Weighting of the Derating Factors

As discussed in Section 3.4, the weighting coefficients of the derating factor $w_{u,l}$ are not chosen uniformly to improve the speed-tracking behavior. Figure 4.11 shows simulation results for uniformly weighting the derating factor in the cost function ($k_w = 0$ in equation (3.13)) for the high-speed test cycle. Compared to Figure 4.7, the derating factor is reduced earlier and the stationary value $f_{\mathrm{drt}} = 0.582$ is lower. Additionally, the permanent magnet temperature is lower and stays around 5 °C below its limit. In this simulated scenario, when using uniform weights, the optimization chooses the derating factors uniformly within the prediction horizon. This entails that the predicted permanent magnet temperature increases steadily and reaches its limit only at the end of the prediction horizon. When the optimization is solved for the next time step, the prediction horizon is shifted. Therefore, the permanent magnet temperature limit is not fully utilized when using equally weighted derating factors. This shows that the weighting coefficients control how conservatively the derating factors are chosen.

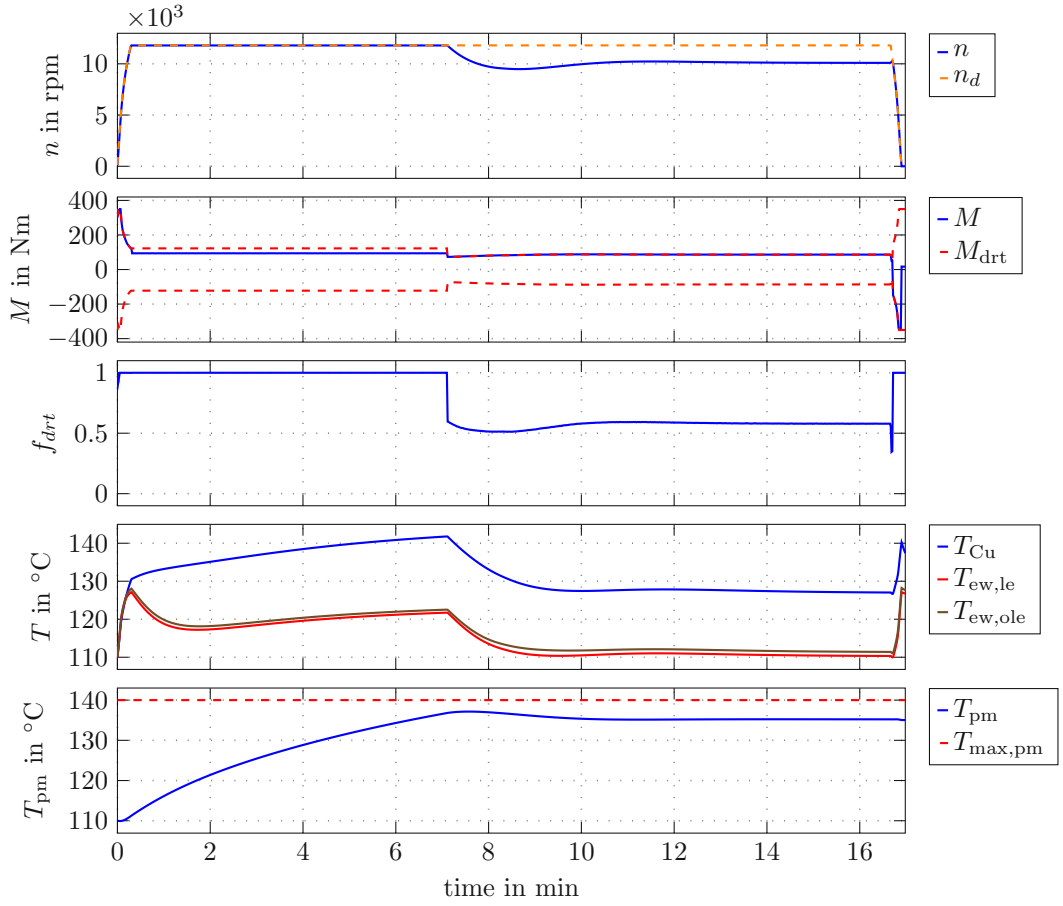

Figure 4.11: Simulation of the high-speed test cycle with MPC-based derating *MPC 1)* with uniform derating factor weights.

Desired Lifetime

The last parameter study shows the effect of the desired lifetime L_d that is used as a reference in the loss-of-life term (3.2) in the MPC cost function. For the simulation results shown in Figure 4.12, the desired lifetime is increased by a factor of 100 to $L'_d = 100 L_d$ compared to Figure 4.9. This means in the optimization that the stator temperatures are weighted stronger than the derating factor. The effect is very noticeable in the resulting lower stator temperatures and the reduced derating factor.

By inverting (3.4) the desired lifetime can be converted to an equivalent reference temperature $T_d = L^{-1}(L_d)$. For the original simulation in Figure 4.9, the reference temperature is $T_d = 170\,°\mathrm{C}$. For the simulation with increased desired lifetime it is $T'_d = 122.5\,°\mathrm{C}$. The stator temperatures in both of these simulations reach approximately the specified reference temperature T_d. The exact reference temperature is not exactly reached, for several reasons including the specific driving cycle, non-uniform weighting of the derating factor, predicted torque and speed and the difference between the three individual stator temperatures corresponding to the active winding and both end-windings.

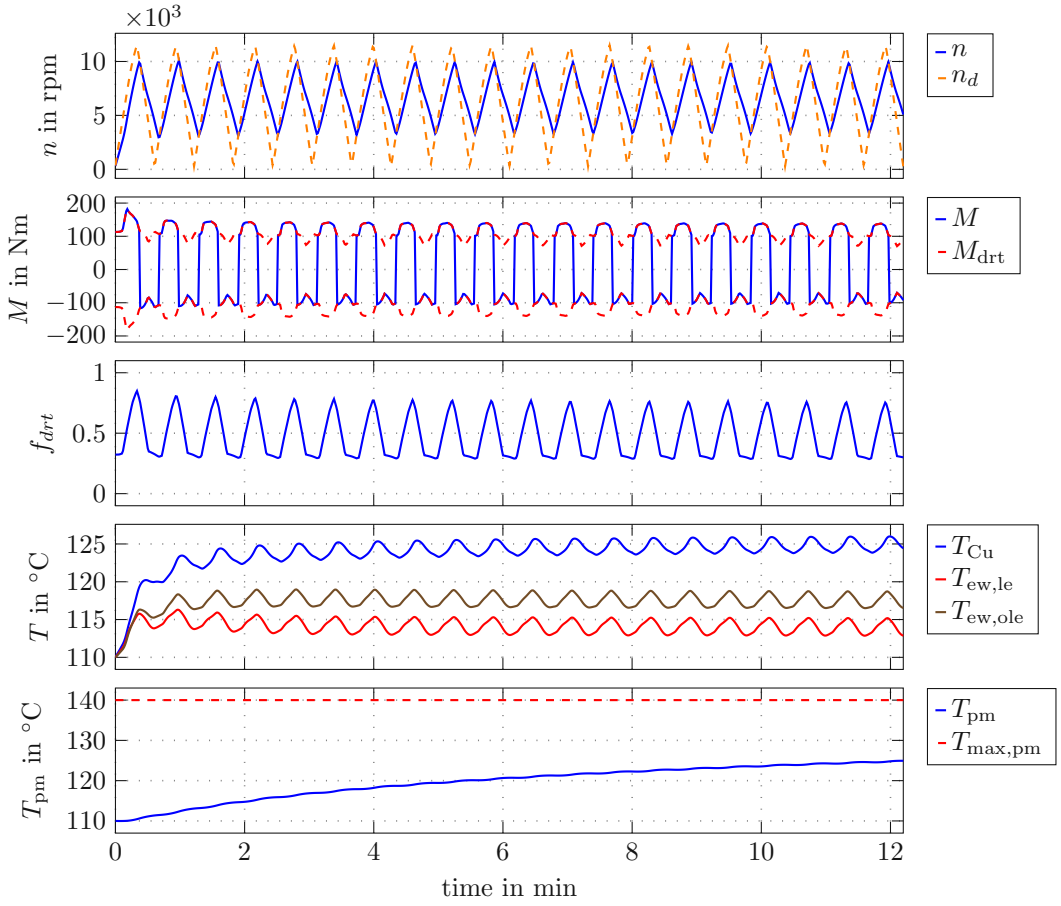

Figure 4.12: Simulation of the stop-and-go test cycle with MPC-based derating *MPC 3)* with increased desired lifetime L_d.

4.3.4 Mountain Road Simulation

As a final example, Figure 4.13 shows the simulated mountain road test cycle using *MPC 1)*. This example represents a realistic driving scenario with changing speed requirements and a varying road slope.

Figure 4.3d shows the motor temperatures without derating. As shown in Figure 4.13, the derating algorithm ensures that the permanent magnet temperature stays within its limit. Figure 4.13 additionally shows the road slope γ and slope estimation error $\Delta\gamma = \hat{\gamma} - \gamma$. The slope estimation, detailed in Section 3.2.1, can follow the actual slope with a small estimation error. The first half of the simulation features some high acceleration phases with lower road slopes. During the second half of the simulation, the desired speed stays constant but there are larger slopes and more changes of the slope. During this second half of the simulation, the derating factor is correlated to the slope. This behavior occurs because the motor speed prediction uses the currently estimated slope for the whole prediction horizon. When the slope is larger, the predicted motor speed increases less, which causes a lower predicted permanent magnet temperature increase and therefore

results in a higher derating factor. Conversely, when the slope is lower the predicted speed increases more during the prediction horizon, causing the temperature to rise faster which in turn results in a lower derating factor.

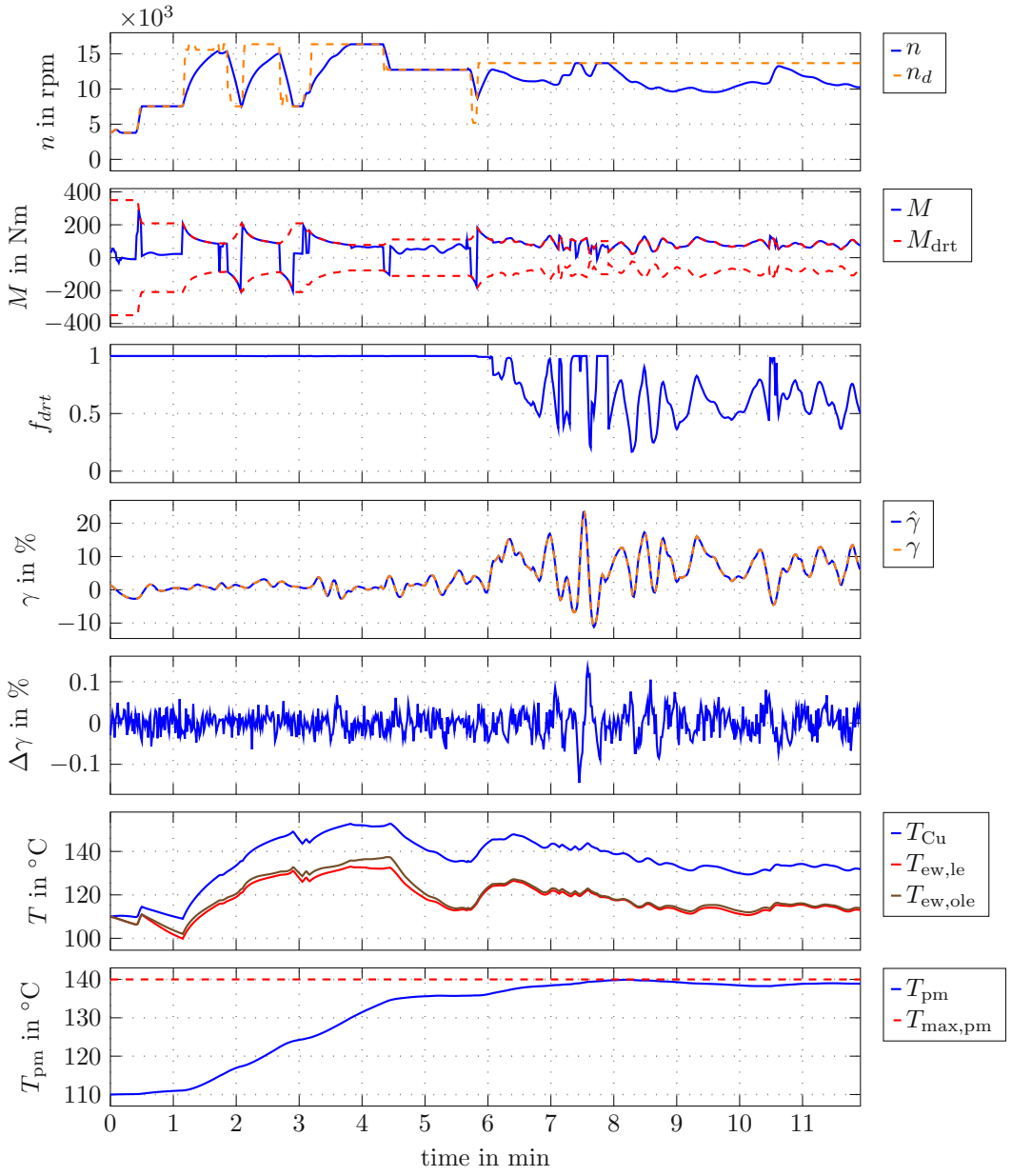

Figure 4.13: Simulation of the mountain road test cycle with MPC-based derating *MPC 1)*.

4.4 Comparison Metrics

To evaluate and compare the simulation results, several performance metrics are used. The MPC-based derating algorithm follows conflicting goals, i. e., maximizing the derating factor, reducing winding degradation, and keeping the temperatures within their limits. The metrics are designed to show how well these goals are achieved by the different derating algorithms and prediction approaches.

The test cycles can take different amounts of time to simulate. Therefore, the total number of steps N_{sim} in each simulation can vary. To simplify comparing the simulation results, the comparison metrics are normalized by N_{sim}.

The derating algorithm computes a derating factor in each step, which limits the maximum available torque. If the desired torque is below this limit, the derating factor does not have any effect. To consider the derating factor only when it has an effect on the applied torque, the effective derating factor

$$f_{\text{drt},e,k} = \begin{cases} f_{\text{drt},k} & \text{if} \quad |M_{d,k}| > M_{\text{drt},k} \\ 1 & \text{otherwise} \end{cases} \tag{4.1}$$

is introduced. The *average effective derating factor*

$$\overline{f_{\text{drt},e}} = \frac{1}{N_{\text{sim}}} \sum_{k=1}^{N_{\text{sim}}} f_{\text{drt},e,k} \ , \tag{4.2}$$

is a measure of the average reduction of the available motor torque to keep temperatures within their limits and to limit the loss of life of the stator windings. The goal of the developed derating algorithm is to better utilize the temperature limits than the state-of-the-art approach using static curves. Therefore, the average effective derating factor $\overline{f_{\text{drt},e}}$ should be higher using the MPC-based derating algorithm.

The loss of life of the stator windings is considered using the *average relative loss of life*

$$\overline{\lambda_{\text{lt}}} = \max_i \left[\frac{1}{N_{\text{sim}}} \sum_{k=1}^{N_{\text{sim}}} \lambda_{\text{lt}}(y_{i,k}) \right] \qquad \text{for } i = 1, 3, 4 \ , \tag{4.3}$$

which is the average of (3.2) over the complete time span of the simulation. Out of the active winding and both end-windings, only the component of the stator windings with the largest loss of life is considered, i. e., the component that degrades the fastest during the respective simulation.

The loss of life factor only applies to the stator windings and not the rotor permanent magnet. The rotor temperature is limited by a hard constraint in the optimization problem. If that constraint is violated, i. e., the optimization does not find an admissible solution, the derating factor is set to zero.

Additionally, the *root mean squared error (RMSE)* for the speed

$$\text{RMSE}(v) = \sqrt{\frac{1}{N_{\text{sim}}} \sum_{k=0}^{N_{\text{sim}}} (v_k - v_{d,k})^2} \tag{4.4}$$

is used to compare the algorithms for the high-speed and stop-and-go test cycles in terms of the tracking performance. This tracking performance is not an explicit goal of the MPC-based derating algorithm. However, it is important in real driving situations and indirectly reflected in the cost function via the derating factor.

4.5 Conclusion

To summarize the results of this chapter, the metrics from Section 4.4 are computed and compared in Table 4.1. Lines with a red background indicate that the permanent magnet temperature limit is exceeded.

For the high-load test cycle (Section 4.5), the speed tracking error is zero and therefore not shown. In the mountain road test cycle, the speed reference is not physically realizable. Hence, the speed tracking error is not meaningful and not shown. Compared to derating using static curves, the MPC-based derating algorithms achieve a higher average derating factor by better utilizing the thermal constraints. This also results in higher temperatures of the stator windings, which means that the average relative loss of life $\overline{\lambda_{\mathrm{lt}}}$ of the MPC-based derating is higher than for static curves.

In the high-speed test cycle, the MPC-based derating can improve the speed tracking performance. However, in the stop-and-go test cycle, the speed tracking error of *MPC 1)* is larger than using static curves, e. g. in Figure 4.8 which shows good speed tracking only at the beginning of the simulation but strongly deteriorates later on. This causes the large speed tracking error shown in Table 4.1c.

Another conclusion from the simulation results is that the prediction method has a major influence on the performance of the MPC-based derating algorithm. From the data, it is not obvious if the approach *MPC 2)* using the assumption of constant speed and peak torque or *MPC 1)* using the prediction based on the mechanical model is the generally better approach for all possible driving conditions. The prediction based on the mechanical model provides better performance and allows for higher torque in the short term, while the other one results in more conservative derating decisions.

algorithm	$\overline{f_{\mathrm{drt},e}}$	$\overline{\lambda_{\mathrm{lt}}}$
no derating	1.000	1.96
static curves	0.618	0.059
MPC 1)	0.767	0.21
MPC 2)	0.779	0.15
MPC 3)	0.835	0.32
MPC P1)	0.763	0.32

(a) High-load test cycle.

algorithm	$\overline{f_{\mathrm{drt},e}}$	$\overline{\lambda_{\mathrm{lt}}}$	RMSE in m/s
no derating	1.000	0.08	0
static curves	0.608	0.02	21.7
MPC 1)	0.796	0.04	10.1
MPC 2)	0.782	0.04	8.9
MPC 3)	0.810	0.04	9.6
MPC P1)	0.827	0.04	8.5
MPC P2)	0.756	0.03	14.7

(b) High-speed test cycle.

algorithm	$\overline{f_{\mathrm{drt},e}}$	$\overline{\lambda_{\mathrm{lt}}}$	RMSE in m/s
no derating	1.000	1.50	0
static curves	0.610	0.08	17.4
MPC 1)	0.719	0.51	36.5
MPC 2)	0.681	0.18	9.5
MPC 3)	0.696	0.17	14.5
MPC P1)	0.823	0.35	12.7
MPC P3)	0.477	1.17	25.3

(c) Stop-and-go test cycle.

algorithm	$\overline{f_{\mathrm{drt},e}}$	$\overline{\lambda_{\mathrm{lt}}}$
no derating	1.000	0.22
static curves	0.649	0.02
MPC 1)	0.827	0.06
MPC 2)	0.824	0.06
MPC P1)	0.837	0.07

(d) Mountain road test cycle.

Table 4.1: Average effective derating factor $\overline{f_{\mathrm{drt},e}}$, average relative loss of life $\overline{\lambda_{\mathrm{lt}}}$, and root mean squared speed tracking error (RMSE) of the various derating and prediction algorithms for the test cycles. Simulations in which the permanent magnet temperature constraint is violated are marked red.
Algorithm abbreviations:
MPC 1) – MPC-based derating using prediction with mechanical model.
MPC 2) – MPC-based derating with constant speed and torque.
MPC 3) – MPC-based derating with known future desired torque and speed.
MPC P1) – Parameter study with prediction horizon $\tau_P = 10\,\mathrm{s}$ (Figure 4.10).
MPC P2) – Parameter study with weight distribution $k_w = 0$ (Figure 4.11).
MPC P3) – Parameter study with desired lifetime $L'_d = 100 L_d$ (Figure 4.12).

5 Conclusions and Outlook

This chapter summarizes the thesis, highlights the limitations behind and assumptions of the presented methods, and discusses possible future improvements and alternative approaches.

5.1 Summary

In this work, a derating algorithm for thermal protection of a permanent magnet synchronous machine is developed based on dynamical models of the vehicle and the motor. For the derating algorithm, the relevant parts of the vehicle are modeled in Chapter 2. The motor models are based on Baumann et al. [15] and include the electrical model, the cooling model, and the reduced-order thermal model. Using the electrical model (Section 2.1), the optimal current setpoint is selected based on the desired motor torque. The modeled motor cooling system (Section 2.3) consists of two cooling circuits, one operates with cooling water and one with oil. Between these two circuits, energy is exchanged by a heat exchanger. The oil flow rate, controlled by the oil pump, and the oil sump temperature are modeled as part of the cooling system. To model the temperature dynamics of the PMSM, a reduced-order model [15] is used. It is based on a high-dimensional finite-volume model of the motor. To make it suitable for real-time evaluation, the model dimension is reduced using model-reduction techniques.

The thermal damage and accelerated aging which can be caused by high temperatures are accounted for in two ways. First, to quantify the degradation of the stator winding insulation (Section 2.5), a lifetime prediction model from [5] is used. Based on this model, the loss of life of the stator windings for a given temperature profile can be measured. Secondly, for the permanent magnet, demagnetization can occur when it is exposed to high temperatures and strong magnetic fields [24]. Both of these damage mechanisms have to be prevented or minimized as part of the thermal protection algorithm.

The vehicle dynamics are modeled using a one-dimensional longitudinal mechanical model, similar to the one used in [11]. This model gives the vehicle position and speed (Section 2.6).

In Chapter 3, the developed thermal protection algorithm is presented and explained. The MPC-based derating algorithm requires knowledge of the future desired motor torque and speed. These quantities are predicted based on the current desired motor torque and road slope using the mechanical vehicle model. The road slope is estimated using an Extended Kalman Filter (Section 3.2.1). The MPC uses the predicted desired motor torque and speed, the thermal motor state and the model of the PMSM to calculate the future thermal state and determine the optimal derating factor. In the cost function of the MPC optimization problem, a compromise between increasing the derating factor and reducing the thermal damage to the stator windings is made (Section 3.4). The

temperature limit of the permanent magnet is enforced using an inequality constraint of the MPC optimization problem.

Section 3.5 contains a discussion on the solution and implementation of the MPC optimization problem. To improve the performance, the model used in the MPC is simplified and optimized for performance.

To validate and test the derating algorithm, simulation studies were conducted, which are presented in Chapter 4. First, the simulation setup is explained and the test cycles used in the simulations are presented. The MPC-based derating is compared to derating based on static derating curves. The comparison shows that using MPC improves the available torque while still keeping the temperatures within their limits. The effects of the different prediction approaches of future desired motor torque and speed are studied. Table 4.1 shows a summary of the simulation results and compares the derating algorithms. Additionally, parameter studies of the prediction horizon length, weighting coefficients for the derating factor in the MPC cost function, and desired lifetime in the loss of life term in the MPC cost function are conducted.

5.2 Limitations

The simulation results show the capabilities of the developed algorithm and its advantages over the derating strategy based on static curves. However, a few limitations also have to be considered. Several simplifying assumptions are made. Only the mentioned components of the vehicle are modeled while other parts are neglected. The battery is not modeled, and its voltage is considered constant. The power electronics, e. g., voltage source inverter, are not modeled. The cooling water flow rate Q_w and input temperature $T_{w,\text{in}}$ are considered constant because the water pump is not included in the model. However, to be on the safe side, the water cooling parameters are selected for a worst-case scenario at high motor temperatures. Q_w is set to its maximum and $T_{w,\text{in}}$ is high as well. Mechanical braking is not modeled, which implies in the simulations that for braking maneuvers less torque is available than in a real vehicle. The mechanical model is only one-dimensional and simplistic, e. g. it assumes that no slip occurs between the road and the wheels. Additionally, other external influences are either not modeled, e. g., wind, or considered constant, e. g., the coefficient of friction of the road and the ambient temperature. Despite these assumptions, the developed derating algorithm has extension points where additional models can be added, e. g., models for the battery or the water pump.

It is assumed that the current thermal state $\mathbf{x}_t$ of the PMSM is known to the MPC-based derating algorithm. In a real implementation, an estimation of the state of the reduced-order model is required, e. g., by using an observer. Additionally, the algorithm is only evaluated using simulations. The model used to represent the plant dynamics is similar to the model used in the MPC-based derating algorithm. For example, the reduced-order model is used to represent the plant dynamics. It is also used in the developed algorithm with the modifications explained in Section 2.7. To evaluate the robustness of the MPC-based derating algorithm, the simulations include noise of the measured motor speed n, the applied torque M, and the measured state $\mathbf{x}_t$ of the reduced-order model.

Another limitation is that the simulations in Chapter 4 were not simulated in real-time.

For implementation on specific hardware, the derating algorithm has to be tuned to achieve real-time performance, e. g., by using the parameter t_{MPC} as explained in Section 3.6.

The next section suggests some improvements and how the mentioned limitations can be overcome.

5.3 Outlook

In this final section, an outlook is given, on how the developed thermal protection algorithm could be improved or extended in the future.

As shown in Chapter 4, the prediction of the future desired motor torque and speed has a considerable influence on the performance of the algorithm. However, in the current approach, only a limited amount of information, i. e., the current desired torque and road slope, is used for this prediction. In many cases, more information about the future driving course is available, e. g., from other sensors or from a navigation system integrated into the vehicle. Sun et al. [28] analyzed the route choice behavior for given start- and end-points based on GPS measurements and created a route prediction model for human drivers. Helmholz et al. [29] predicted the future route trajectory for cases when the end-point is unknown to the car (i. e., without an active navigation system) based on the driver's travel history. Another approach, specific for use by MPC applications, is examined by Mohammadi et al. [27]. Using an artificial neural network, the future inputs from a human driver are predicted, to improve the performance of the MPC.

Next, the limitation that the simulation model is very similar to the model used in the algorithm is addressed. This limitation could be compensated if a better, more sophisticated simulation environment was used that utilizes more accurate and complex plant models. There exist various simulation tools for use in the automotive industry that allow more realistic simulations, such as IPG CarMaker[1], CarSim[2], or AVL Cruise M[3]. Additionally, some of these tools also include controllers that mimic the behavior of human drivers.

Finally, the limitations due to the computational performance are discussed. To facilitate real-time capabilities, the models, especially the thermal model, as well as the optimization problem, as discussed in Section 3.5, would have to be modified to be more performant to evaluate. Then, the mechanical model could be included in the MPC to allow for a different cost function that could directly weigh the vehicle speed (see Section 3.4). Additionally, the prediction of future motor torque and speed could be included into the MPC so that the derating factor influences the predicted values within the optimization problem.

[1] https://ipg-automotive.com/en/products-solutions/software/carmaker/
[2] https://www.carsim.com/products/carsim/
[3] https://www.avl.com/en/simulation-solutions/software-offering/simulation-tools-z/avl-cruise-m

A Calculations

A.1 Non-Uniform Derating Factor Weighting

This appendix explains the weighting coefficients $w_{u,l}$ of the derating factor introduced in Section 3.4. Because the MPC does not include the mechanical model, it is not possible to use the vehicle position, vehicle speed, or time to travel a certain distance in the MPC cost function. The following derivations aim to maximize the traveled distance s_N, even though it cannot be explicitly included in the cost function.

The non-uniform weight distribution of the derating factor in the cost function is selected based on the mechanical vehicle model and some simplifying assumptions. The assumptions are:

- The acceleration is approximately proportional to the applied torque $a = \dot{v} \propto M_m$.
- The acceleration is piecewise constant $a(l\tau_C) = a_l$ for intervals of the step size τ_C.
- The driving duration is fixed and a multiple of the step size $t_{\text{tot}} = N\tau_C$.
- The initial conditions for position and speed are $s_0 = 0$ and $v_0 = 0$, respectively.

The position at the end of the driving duration is

$$s(t_{\text{tot}}) = s_N = \iint_0^{t_{\text{tot}}} a(t)\,\mathrm{d}t^2 = \tau_C \sum_{l=0}^{N-1} \overline{v}_{l,l+1} \ , \tag{A.1}$$

using the average speed $\overline{v}_{l,l+1}$ during a sampling period. The speed at the start of a time step reads as

$$v(l\tau_C) = v_l = \int_0^{l\tau_C} a(t)\,\mathrm{d}t = \tau_C \sum_{i=0}^{l-1} a_i \ . \tag{A.2}$$

The average speed during a time step follows as

$$\overline{v}_{l,l+1} = \frac{v_l + v_{l+1}}{2} = \tau_C \left[\frac{a_l}{2} + \sum_{i=0}^{l-1} a_i \right] . \tag{A.3}$$

Using (A.1) and (A.3), the final position

$$s_N = \tau_C^2 \sum_{l=0}^{N-1} \frac{2(N-l-1)+1}{2} a_l \tag{A.4}$$

can be calculated as a function of the acceleration values. This shows that, the influence of the acceleration a_l on the final position s_N is

$$\frac{\mathrm{d}s_N}{\mathrm{d}a_l} = \tau_C^2 \frac{2(N-l-1)+1}{2} \ . \tag{A.5}$$

This influence decreases linearly with time. When normalized by

$$\sum_{l=0}^{N-1} \frac{\mathrm{d}s_n}{\mathrm{d}a_l} = \frac{\tau_C^2 N^2}{2} \ , \tag{A.6}$$

this results in the second part of the weighting factor (3.13)

$$w_{u2,l} = \frac{2(N-l-1)+1}{N^2} \ , \tag{A.7}$$

which is stage-dependent.

The first term $w_{u1,l} = \frac{1}{N}$ in (3.13) is constant, which finally gives

$$w_{u,l} = \frac{1-k_w}{N} + k_w \frac{2(N-1-l)+1}{N^2} \ . \tag{3.13}$$

The weight distribution factor k_w allows balancing the importance of the first and second terms. It was found that a value of $k_w = 0.8$ achieves a good compromise between short-term and long-term performance.

Bibliography

[1] IEA, "Global EV outlook 2021," International Energy Agency, Paris, France, 2021.

[2] J. De Santiago, H. Bernhoff, B. Ekergård, S. Eriksson, S. Ferhatovic, R. Waters, and M. Leijon, "Electrical motor drivelines in commercial all-electric vehicles: A review," *IEEE Transactions on Vehicular Technology*, vol. 61, no. 2, pp. 475–484, Feb. 2012, ISSN: 1939-9359.

[3] J. Brady and M. O'Mahony, "Development of a driving cycle to evaluate the energy economy of electric vehicles in urban areas," *Applied Energy*, vol. 177, pp. 165–178, Sep. 2016, ISSN: 03062619.

[4] IEC 60085:2007, *Electrical insulation - thermal evaluation and designation*, International Electrotechnical Commission, Nov. 2007.

[5] V. Madonna, C. Spagnolo, P. Giangrande, and M. Galea, "Improving performance and extending lifetime of PMSMs via advanced end-winding cooling," in *2020 IEEE 29th International Symposium on Industrial Electronics (ISIE)*, Delft, Netherlands: IEEE, Jun. 2020, pp. 319–325, ISBN: 978-1-72815-635-4.

[6] T. Sebastian, "Temperature effects on torque production and efficiency of PM motors using NdFeB magnets," in *Conference Record of the 1993 IEEE Industry Applications Conference Twenty-Eighth IAS Annual Meeting*, Toronto, Ont., Canada: IEEE, 1993, pp. 78–83, ISBN: 978-0-7803-1462-7.

[7] T. Engelhardt, *Derating-Strategien für elektrisch angetriebene Sportwagen*. Wiesbaden, Germany: Springer Fachmedien Wiesbaden, 2017, ISBN: 978-3-658-18207-6.

[8] J. Lemmens, P. Vanassche, and J. Driesen, "Optimal control of traction motor drives under electrothermal constraints," *IEEE Journal of Emerging and Selected Topics in Power Electronics*, vol. 2, no. 2, pp. 249–263, Jun. 2014, ISSN: 2168-6785.

[9] G. Lo Calzo, A. Lidozzi, L. Solero, F. Crescimbini, and V. Cardi, "Thermal regulation as control reference in electric drives," in *2012 15th International Power Electronics and Motion Control Conference (EPE/PEMC)*, Novi Sad, Serbia: IEEE, Sep. 2012, pp. 676–682, ISBN: 978-1-4673-1972-0.

[10] L. Grüne and J. Pannek, *Nonlinear Model Predictive Control*. Springer International Publishing, 2017, ISBN: 978-3-319-46024-6.

[11] O. Wallscheid and J. Böcker, "Derating of automotive drive systems using model predictive control," in *2017 IEEE International Symposium on Predictive Control of Electrical Drives and Power Electronics (PRECEDE)*, Pilsen, Czech Republic: IEEE, Sep. 2017, pp. 31–36, ISBN: 978-1-5386-0507-3.

[12] A. Winkler, J. Frey, T. Fahrbach, G. Frison, R. Scheer, M. Diehl, and J. Andert, "Embedded real-time nonlinear model predictive control for the thermal torque derating of an electric vehicle," *IFAC-PapersOnLine*, vol. 54, no. 6, pp. 359–364, 2021, ISSN: 24058963.

[13] T. Sun, J. Wang, A. Griffo, and B. Sen, "Active thermal management for interior permanent magnet synchronous machine (IPMSM) drives based on model predictive control," *IEEE Transactions on Industry Applications*, vol. 54, no. 5, pp. 4506–4514, Sep. 2018, ISSN: 1939-9367.

[14] O. Wallscheid, "Thermal monitoring of electric motors: State-of-the-art review and future challenges," *IEEE Open Journal of Industry Applications*, vol. 2, pp. 204–223, 2021, ISSN: 2644-1241.

[15] M. S. Baumann, A. Steinböck, W. Kemmetmüller, and A. Kugi, *Real-time capable thermal model of a permanent magnet synchronous machine*, submitted to IEEE Open Journal of the Industrial Electronics Society, 2024.

[16] H. Ohnishi, "A study on road slope estimation for automatic transmission control," *JSAE Review*, vol. 21, no. 2, pp. 235–240, Apr. 2000, ISSN: 03894304.

[17] P. Lingman and B. Schmidtbauer, "Road slope and vehicle mass estimation using Kalman filtering," *Vehicle System Dynamics*, vol. 37, pp. 12–23, Jan. 2002, ISSN: 1744-5159.

[18] M. N. Mahyuddin, J. Na, G. Herrmann, X. Ren, and P. Barber, "Adaptive observer-based parameter estimation with application to road gradient and vehicle mass estimation," *IEEE Transactions on Industrial Electronics*, vol. 61, no. 6, pp. 2851–2863, Jun. 2014, ISSN: 1557-9948.

[19] Vincent Winstead and Ilya V. Kolmanovsky, "Estimation of road grade and vehicle mass via model predictive control," in *Proceedings of 2005 IEEE Conference on Control Applications, 2005. CCA 2005.*, Toronto, Canada: IEEE, 2005, pp. 1588–1593, ISBN: 978-0-7803-9354-7.

[20] Bing Cheng and T. Tesch, "Torque feedforward control technique for permanent-magnet synchronous motors," *IEEE Transactions on Industrial Electronics*, vol. 57, no. 3, pp. 969–974, Mar. 2010, ISSN: 0278-0046.

[21] B. Bilgin, J. Liang, M. V. Terzic, J. Dong, R. Rodriguez, E. Trickett, and A. Emadi, "Modeling and analysis of electric motors: State-of-the-art review," *IEEE Transactions on Transportation Electrification*, vol. 5, no. 3, pp. 602–617, Sep. 2019, ISSN: 2332-7782.

[22] S. Gugercin, A. C. Antoulas, and C. Beattie, "$\mathcal{H}_2$ model reduction for large-scale linear dynamical systems," *SIAM Journal on Matrix Analysis and Applications*, vol. 30, no. 2, pp. 609–638, Jan. 2008, ISSN: 1095-7162.

[23] A. Bruns and P. Benner, "Parametric model order reduction of thermal models using the bilinear interpolatory rational Krylov algorithm," *Mathematical and Computer Modelling of Dynamical Systems*, vol. 21, no. 2, pp. 103–129, Mar. 4, 2015, ISSN: 1387-3954.

[24] K.-C. Kim, S.-B. Lim, D.-H. Koo, and J. Lee, "The shape design of permanent magnet for permanent magnet synchronous motor considering partial demagnetization," *IEEE Transactions on Magnetics*, vol. 42, no. 10, pp. 3485–3487, Oct. 2006, ISSN: 0018-9464.

[25] T. W. Dakin, "Electrical insulation deterioration treated as a chemical rate phenomenon," *Transactions of the American Institute of Electrical Engineers*, vol. 67, no. 1, pp. 113–122, Jan. 1948, ISSN: 0096-3860.

[26] X. Liao, Q. Huang, D. Sun, W. Liu, and W. Han, "Real-time road slope estimation based on adaptive extended Kalman filter algorithm with in-vehicle data," in *2017 29th Chinese Control And Decision Conference (CCDC)*, Chongqing, China: IEEE, May 2017, pp. 6889–6894, ISBN: 978-1-5090-4657-7.

[27] A. Mohammadi, H. Asadi, S. Mohamed, K. Nelson, and S. Nahavandi, "Future reference prediction in model predictive control based driving simulators," in *2016 Australasian conference on robotics and automation (ACRA2016)*, Canberra, Australia, Dec. 2016, pp. 177–184.

[28] D. Sun, C. Zhang, L. Zhang, F. Chen, and Z.-R. Peng, "Urban travel behavior analyses and route prediction based on floating car data," *Transportation Letters*, vol. 6, no. 3, pp. 118–125, Jul. 2014, ISSN: 1942-7875.

[29] P. Helmholz, E. Ziesmann, and S. Robra-Bissantz, "Context-awareness in the car: Prediction, evaluation and usage of route trajectories," in *Design Science at the Intersection of Physical and Virtual Design*, vol. 7939, Berlin, Heidelberg: Springer Berlin Heidelberg, 2013, pp. 412–419, ISBN: 978-3-642-38827-9.

Eidesstattliche Erklärung

Hiermit erkläre ich, dass die vorliegende Arbeit gemäß dem Code of Conduct - Regeln zur Sicherung guter wissenschaftlicher Praxis (in der aktuellen Fassung des jeweiligen Mitteilungsblattes der TU Wien), insbesondere ohne unzulässige Hilfe Dritter und ohne Benutzung anderer als der angegebenen Hilfsmittel, angefertigt wurde. Die aus anderen Quellen direkt oder indirekt übernommenen Daten und Konzepte sind unter Angabe der Quelle gekennzeichnet. Die Arbeit wurde bisher weder im In- noch im Ausland in gleicher oder in ähnlicher Form in anderen Prüfungsverfahren vorgelegt.

Wien im Februar 2024

Andreas Fischer